Mon. Not. R. Astron. Soc. **000**, 1–20 (2013) Printed 8 July 2014 (MN LATEX style file v2.2)

A high resolution study of complex organic molecules in hot cores

Hannah Calcutt[1]*, Serena Viti[1], Claudio Codella[2], Maria T. Beltrán[2], Francesco Fontani[2], Paul M. Woods[1,3]

[1] *Department of Physics and Astronomy, University College London, WC1E 6BT, London, UK*
[2] *INAF, Osservatorio Astrofisico di Arcetri, Largo Enrico Fermi 5, I-50125 Firenze, Italy*
[3] *Astrophysics Research Centre, School of Mathematics & Physics, Queen's University Belfast, Belfast BT7 1NN, UK*

ABSTRACT

We present the results of a line identification analysis using data from the IRAM Plateau de Bure Inferferometer, focusing on six massive star-forming hot cores: G31.41+0.31, G29.96-0.02, G19.61-0.23, G10.62-0.38, G24.78+0.08A1 and G24.78+0.08A2. We identify several transitions of vibrationally excited methyl formate ($HCOOCH_3$) for the first time in these objects as well as transitions of other complex molecules, including ethyl cyanide (C_2H_5CN), and isocyanic acid (HNCO). We also postulate a detection of one transition of glycolaldehyde ($CH_2(OH)CHO$) in two new hot cores. We find G29.96-0.02, G19.61-0.23, G24.78+0.08A1 and G24.78+0.08A2 to be chemically very similar. G31.41+0.31, however, is chemically different: it manifests a larger chemical inventory and has significantly larger column densities. We suggest that it may represent a different evolutionary stage to the other hot cores in the sample, or it may surround a star with a higher mass. We derive column densities for methyl formate in G31.41+0.31, using the rotation diagram method, of 4×10^{17} cm^{-2} and a T_{rot} of ∼170 K. For G29.96-0.02, G24.78+0.08A1 and G24.78+0.08A2, glycolaldehyde, methyl formate and methyl cyanide all seem to trace the same material and peak at roughly the same position towards the dust emission peak. For G31.41+0.31, however, glycolaldehyde shows a different distribution to methyl formate and methyl cyanide and seems to trace the densest, most compact inner part of hot cores.

Key words: ISM: molecules — ISM: abundances — Astrochemistry — stars: formation — stars: protostars — line: identification

1 INTRODUCTION

The process that leads to the formation of a high-mass star, whether it is by accretion (McKee & Tan 2002, 2003), or coalescence and accretion (Bonnell et al. 1998) is extremely fast, $\sim10^4$–10^5 yr, and will, according to some evolutionary models, depend on the final mass of the star (e.g., Bernasconi & Maeder 1996). The contraction of a core from a low to a very high density ($\sim10^7$ cm^{-3}) occurs very quickly and the star will reach the Zero Age Main Sequence while still embedded (Palla & Stahler 1993). This, together with the fact that massive stars tend to form in association, makes the determination of the early stages of the evolution of a massive star via observations of Spectral Energy Distributions (SEDs) a rather difficult task.

A common way of observing massive young stellar objects (YSOs) has been via the detection of hypercompact and ultracompact HII regions (UCHII): regions of dense gas ionized by the newly formed star. However, ionised regions trace relatively late evolutionary stages. On the other hand, the earliest phases are well traced by hot cores, which are small ($\sim10^{-2}$–10^{-1} pc), dense ($\geqslant10^7$ cm^{-3}), relatively warm ($\geqslant10^2$ K), optically thick ($A_v\geqslant10^2$ mag), and transient ($\leqslant10^5$ yr) condensations. Spectral surveys have revealed a very rich chemistry (see review by Herbst & van Dishoeck (2009); Garay & Lizano (1999)) which include high abundances of small saturated molecules (e.g. H_2O, NH_3, H_2S, CH_3OH) as well as large organic species (CH_3CN, CH_2CHCN, CH_3CH_2CN, C_2H_5OH). Such high abundances are believed to arise from the sublimation of ice mantles frozen out onto the dust grains during the collapse of the parent cloud, which is induced by the nearby (proto)star.

* E-mail: hcalcutt@star.ucl.ac.uk

Once the protostar is born, the dust is heated and molecules formed on the dust grain sublimate. This warm-up phase is most likely not instantaneous (Viti & Williams 1999); (Viti et al. 2004); (Garrod et al. 2008), and there is experimental evidence that desorption occurs in as many as four stages in four distinct narrow temperature ranges (temperature bands). The proportion of each species that evaporates in each band depends on the total amount present on the grains as well as on the bonding properties of the molecule (Collings et al. 2004). Chemical models incorporating such experimental results show that distinct chemical events occur at specific grain temperatures and these differ depending on the mass of the star (Viti et al. 2004). The chemistry of the hot cores will, therefore, reflect this temperature-driven evolution and the evolutionary chemistry can provide, in principle, a record of the collapse process as well as the ignition history of the star.

Of course, since there is a chemical differentiation over time due to a time-dependent increase of the dust temperature, one also expects a space-dependent chemical differentiation due to the difference in dust temperature progressively further away from the star. The degeneracy between time and spatial effects can only be solved by interferometric observations and chemical modelling. A class of molecules that can be particularly useful to solve this degeneracy is that of complex organic molecules (COMs) because (i) their detection is a confirmation of the high density warm cores, as most COMs are not easily produced in the gas phase chemistry of dark clouds and, ii) most importantly, their emission has been observed to be compact in extent in star forming regions outside the Galactic Center (Herbst & van Dishoeck 2009; Garay & Lizano 1999) and therefore may trace the most central region of the hot core, close to the YSOs. In fact, many organic molecules have been detected in hot cores and have been used to trace different structures associated with star formation such as discs and maser activity (e.g. Olmi et al. 1996; Cesaroni et al. 1998; Olmi et al. 2003; Beltrán et al. 2005, 2011). Multi-transition and multi-species observations of complex molecules are essential in order to derive the temperature and excitation conditions of hot cores, especially if different transitions and species trace different extensions of the core.

Beltrán et al. (2005) mapped the CH_3CN emission in two hot cores and spectrally identified many other organic molecules in both objects. This work led to the first detection outside the Galactic Centre of a transition of glycolaldehyde, $CH_2(OH)CHO$, in G31.41+0.31 (Beltrán et al. 2009). The richness of these spectra gives a great insight into the chemistry of this type of object, which we investigate in depth here. In addition to the previously-published data for G31.41+0.31 and G24.78+0.08 A2, we also analyse the unpublished spectra of four more hot cores to give a sample of six (see Sect. 2). Seven emission lines evaded definite identification in the spectrum of G31.41+0.31 at 1.4 mm. In this paper we identify some of these unidentified lines, and find that they are seen in other members of our sample. Since all the new identifications are of complex species, we use the new data in conjunction with previously-published data to derive the excitation conditions of each core. We then make use of a chemical model of a hot core to interpret the molecular inventory of the six cores and qualitatively characterise each core and its evolutionary stage. Previous work such as Isokoski et al. (2013) have taken a molecular inventory of hot cores using single dish observations to look for chemical differences in objects with disk-like structures compared to those without disks. This work will explore the chemical differences between hot cores by making use of high spatial resolution observations. This will allow us to look at the spatial chemical variation in hot cores as well as the variability between objects.

2 OBSERVATIONS

This work is based on observations taken with the Plateau de Bure Interferometer (PdBI) and reported by Beltrán et al. (2005), for the hot cores G31.41+0.31 (G31) and A1 and A2 in G24.78+0.08 (G24A1 and G24A2), and by Beltrán et al. (2011) for the hot cores G29.96-0.02 (G29), G19.61-0.23 (G19), G10.62-0.38 (G10). Information about the observations can be found in their Section 2. The synthesized CLEANed beams for maps made using natural weighting can be found in Table 1. The V_{LSR} for each hot core listed in Table 1 has been determined from high spatial resolution observations of the 12-13 transitions of $CH_3{}^{13}CN$.

These observations range from 220 209.95 MHz to 220 759.69 MHz for all the hot cores and were analysed using the GILDAS software package. [1]

3 THE SAMPLE OF HOT CORES

We have selected luminous ($L_{\rm bol} > 10^4\,L_\odot$) objects with typical signposts of massive star formation such as water masers and ultracompact (UC) HII regions.

Six hot cores were observed towards five star-forming regions on the basis of being bright in the sub-mm, and having previously given indications of being chemically rich. We discuss each source in detail below.

G31.41+0.31: This is a well-studied hot core located at 7.9 kpc (Cesaroni et al. 1994, 1998), with evidence of a rotating massive molecular toroid, suggested by OH maser emission and confirmed using CH_3CN emission (Gaume & Mutel 1987; Beltrán et al. 2004, 2005; Cesaroni et al. 2011). It has been mapped in several different molecules including SiO, HCO^+ and NH_3, as well as several complex molecules like CH_3CN, C_2H_5CN and $CH_2(OH)CHO$ (Cesaroni et al. 1994; Maxia et al. 2001; Beltrán et al. 2005). Interferometric observations of molecular lines with high excitation energies have revealed the presence of deeply-embedded YSOs, which in all likelihood explains the temperature increase toward the core centre (Beltrán et al. 2004, 2005; Cesaroni et al. 2010). The Spitzer/GLIMPSE images by Benjamin (2003) show that the G31 hot core lies in a complex parsec-scale region where both extended emission and multiple stellar sources are detected.

G29.96-0.02: G29 is located at a distance of 3.5 kpc (Beltrán et al. 2011) and associated with the infrared source IRAS 18434-0242. It contains a cometary UCHII region with a hot core located in front of the cometary arc (Wood & Churchwell 1989; Cesaroni et al. 1994). It has been mapped in several molecules including NH_3, HCO^+,

[1] http://www.iram.fr/IRAMFR/GILDAS

Table 1. Parameters of the IRAM PdBI observations

Source	α(J2000)† (h m s)	δ(J2000) ($^\circ$ $'$ $''$)	V_{LSR} (kms^{-1})	Synthesized Beam †† ($''$)	P.A. ($^\circ$)	Velocity resolution (kms^{-1})
G31.41+0.31	18 47 34.330	-01 12 46.50	96.8[a]	1.1 × 0.5	-170	3.4
G29.96-0.02	18 46 03.955	-02 39 21.87	98.9[b]	1.4 × 0.7	168	3.4
G19.61-0.23	18 27 38.145	-11 56 38.49	41.6[b]	2.6 × 1.0	161	3.4
G10.62-0.38	18 10 28.650	-19 55 49.50	-2.0[b]	2.4 × 0.7	169	3.4
G24.78+0.08	18 36 12.660	-07 12 10.15	110.8[a]	1.2 × 0.5	-174	3.4

† Coordinates of the phase centre of the observations.
†† The synthesized CLEANed beams for maps made using natural weighting.
[a]Beltrán et al. (2005)
[b]Beltrán et al. (2011)

CS, CH_3CN, HNCO and $HCOOCH_3$ (Cesaroni et al. 1998; Pratap et al. 1999; Maxia et al. 2001; Olmi et al. 2003; Beuther et al. 2007). A velocity gradient along the east-west direction has been measured in NH_3, CH_3CN, and $HN^{13}C$ emission which is interpreted as rotation (Cesaroni et al. 1998; Olmi et al. 2003; Beuther et al. 2007). On the other hand, an outflow directed along the southeast-northwest direction has been mapped in H_2S and SiO by Gibb et al. (2004) and Beuther et al. (2007). Beltrán et al. (2001) confirmed the existence of a rotating molecular toroid around the outflow axis. Masers of H_2O, CH_3OH and H_2CO have also been detected around this hot core (Hofner & Churchwell 1996; Walsh et al. 1998; Hoffman et al. 2003).

G19.61-0.23: G19 is located at a distance of 12.6 kpc (Kolpak et al. 2003), and associated with the infrared source IRAS 18248-1158. It contains several embedded UCHII regions, detected by Garay et al. (1985), and more recently mapped by Furuya et al. (2005). Several molecular tracers, such as CS, NH_3, CH_3CH_2CN, $HCOOCH_3$, and CH_3CN have been mapped in this hot core (Plume et al. 1992; Garay et al. 1998; Remijan et al. 2004; Furuya et al. 2005). ^{13}CO and $C^{18}O$ emission show inverse P Cygni profiles indicating infalling gas towards the core (Wu et al. 2009; Furuya et al. 2011). López-Sepulcre et al. (2009) mapped a ^{13}CO outflow without a well-defined morphology. H_2O, OH, and CH_3OH masers have been detected by Forster & Caswell (1989), Hofner & Churchwell (1996) and Walsh et al. (1998). Beltrán et al. (2011) reported velocity gradients, observed in CH_3CN, oriented perpendicular to the direction of a molecular outflow.

G10.62-0.38: G10 is located at a distance of 3.4 kpc (Blum et al. 2001) and contains a well-studied UCHII region (e.g. Wood & Churchwell 1989) associated with the infrared source IRAS 18075-1956. The hot core in this star forming region has been mapped in NH_3 (Ho & Haschick 1986; Keto et al. 1987, 1988; Sollins & Ho 2005) and in SO_2 and OCS (Klaassen et al. 2009). Infall and bulk rotation in the molecular gas surrounding the UCHII region have been detected. H66α emission shows the occurrence of inward motions in the ionised gas (Keto 2002). CH_3OH and H_2O masers have been mapped towards the core and are distributed linearly in the plane of the rotation (Hofner & Churchwell 1996; Walsh et al. 1998), while OH masers appear to lie along the axis of rotation (Argon et al. 2000). Outflow activity has been detected by Keto & Wood (2006), López-Sepulcre et al. (2009) and by Beltrán et al. (2011), who reported a CH_3CN toroid rotating around the main axis of the outflow.

G24.78+0.08A1 and G24.78+0.08A2: G24 is a high-mass star-forming region located at 7.7 kpc from the Sun, and associated with several YSOs in different evolutionary phases embedded in their parental cores (Furuya et al. 2002). The G24 region has been extensively studied in various molecules like CO, NH_3 and CS, as well as in complex molecules and in the continuum (Codella et al. 1997; Cesaroni et al. 2003; Beltrán et al. 2005, 2011). Two main groups of YSOs, called A1 and A2, are separated by $\sim$1$''$.5 (Beltrán et al. 2011, and references therein). *G24.78+0.08A1:* G24A1 is one of the three massive cores with a rotating toroid detected in G24 (Beltrán et al. 2011). At the centre of G24A1, an unresolved hypercompact (HC) HII region is created by a YSO with a spectral type of at least O9.5 (Codella et al. 1997; Beltrán et al. 2007). NH_3 (2,2) observations have revealed that the gas in the toroid is undergoing infall towards the HC HII region (Beltrán et al. 2006), suggesting that accretion onto the star might still be occurring, even through the ionised region (for a potential mechanism, see Keto & Wood 2006). On the other hand, Very Long Baseline Array proper motion measurements of H_2O masers associated with the HC HII region (Moscadelli et al. 2007) indicate that the ionised region might be expanding, thus questioning the possibility of accretion onto the star. *G24.78+0.08A2:* G24A2 is also associated with a massive CH_3CN toroid, rotating around the main axis of a bipolar outflow observed in the CO isotopologues (Furuya et al. 2002; Beltrán et al. 2005, 2011; Codella et al. 2013). The mid-infrared and radio continuum measurements show a compact (1000–2000 AU) source which could be due to an ionised jet (Vig et al. 2008). Emission from several complex molecules clearly indicate the presence of a molecular hot core (Beltrán et al. 2005, 2011; Codella et al. 2013).

4 MOLECULAR CONTENT

Figure 1 shows the reduced spectrum for each hot core; we label the identified lines (Beltrán et al. 2005) as well as the seven unidentified lines in G31, A to G in ascending frequency in the top panel. As can be seen from the figure, not all lines are present in all cores. Lines C, D, F and G were too blended with other lines to be clearly identified. Table 4 lists the previously unidentified lines which could be identi-

fied (A, B and E), with their frequencies and observational parameters, and which cores they are detected in. These will be discussed in Sect. 4.2.

We also find that several of the molecular lines identified in G31, G24A1 and G24A2 by Beltrán et al. (2005) are also seen in other members of our sample of hot cores. We briefly discuss these new detections in Sect. 4.1.

We determine the identity of all of the spectral lines in our sample using a rigorous method to avoid misidentifications. Here we follow the line identification process as presented in Snyder et al. (2005). While we refer the reader to the Snyder et al. (2005) paper for a detailed explanation of the recipe one has to follow in order to identify a spectral line, here we very briefly summarise the criteria used:

(i) We only considered transitions with a frequency error of <50 MHz.
(ii) All the expected transitions of a molecule must have frequency agreement. In the case of line blending two lines should be at least resolved by the Rayleigh criterion. Snyder et al. (2005) also remark that a more stringent criterion may be used whereby two overlapping lines can be considered to be resolved if they are least separated at the half-maximum intensity of the weakest line.
(iii) If other transitions from the same molecule are present in the observed frequency range, have line strengths at detectable levels, and there are no mitigating circumstances such as maser activity or line self-absorption as to why they should not be observed, they should be present in the spectra. Their relative intensity must also correspond to the predicted one under LTE.
(iv) Transitions from molecules already observed in similar objects and, if not, in the interstellar medium (ISM), should be favoured over new molecules not yet detected in space.
(v) Excluding transitions with upper energy levels exceeding the highest upper energy level of a transition previously detected in the hot core sample (931 K).

We have used the JPL, CDMS, and Lovas/NIST molecular spectroscopy databases for line identification [2]. We find that there are uncertainties in both the frequencies of lines in the molecular databases and the observed frequency of the unidentified astronomical lines. Any line with a measured laboratory frequency uncertainty larger than 50 MHz has been excluded from consideration. Since the spectral resolution of the observations is 2.5 MHz, we searched for lines within the linewidths of the unidentified lines. The list of potential lines has been reduced by excluding transitions with an upper energy level over 931 K, as typically excitation temperatures of the present hot core sample do not exceed ∼300 K (e.g. Beltrán et al. 2005; Beltràn et al. 2010, and references therein) and to date, the highest upper energy level of a transition previously detected in the hot core sample is 931 K.

4.1 New detections

In this subsection we identify lines in the G10, G19 and G29 hot cores, which have already been detected in G31, and in most cases already detected in G24A1 and G24A2 as well. Table 2 shows the derived frequency, velocity, integrated intensity, FWHM, peak temperature and rms of the baseline for these newly detected lines in each hot core and the transitional information can be found in Table 3.

The $10_{1,9}$–$9_{1,8}$ transition of HNCO is detected in a further two hot cores, G19 and G29 (see Fig. 2), although it is blended with one transition of methyl cyanide in all cores.

The $25_{2,24}$–$24_{2,23}$ transition of C_2H_5CN was also detected in G31, G24A1 and G24A2 in Beltrán et al. (2005). We have found it in a further two hot cores: G19 and G29 (Fig. 3). This line is very bright in G31 at 19.7 K but is as weak as 4.0 K in G29. The FWHM is similar in all the hot cores, ranging from 6.9 kms^{-1} in G29 to 10.8 kms^{-1} in G19. It is not detected in G10. Both of these lines are brightest in G31.

4.1.1 Glycolaldehyde ($CH_2(OH)CHO$)

The complex organic molecule glycolaldehyde (CH_2OHCHO), which is an isomer of both methyl formate ($HCOOCH_3$) and acetic acid (CH_3COOH), is the simplest of the monosaccharide sugars. This important organic molecule was first tentatively detected at 1.4 mm with the PdBI outside the Galactic centre, where it was observed in Sgr B2(N) (Hollis et al. 2000) towards three massive hot-cores (G31, G24A1, and G24A2) by Beltrán et al. (2005). Later on, Beltrán et al. (2009) confirmed the detection by observing two additional Glycolaldehyde transitions towards G31 at 2.1 and 2.9 mm with the PdBI. Recently, Jørgensen et al. (2012) have detected 13 transitions towards the Class 0 IRAS 16293–2422 object at 0.4 and 1.4 mm, using the ALMA array towards the hot-corino surrounding the Solar-type protostar.

In this present work, we report a new detection of a line at ∼220 466 MHz in two hot cores (Fig. 4), G29 (3σ detection) and G19 (5σ detection), which we postulate to be the $20_{2,18}$–$19_{3,17}$ transition of glycolaldehyde, as was detected by Beltrán et al. (2005) in G31, G24A1 and G24A2. We observe a shift in the velocity of 3-4 km/s in this transition compared to the V_{LSR} of each hot core. This is consistent with the glycolaldehyde observations of both Beltrán et al. (2009), Halfen et al. (2006), and Hollis et al. (2000). Whilst further transitions of this molecule are needed to confirm its presence within G29 and G19, if confirmed, it would suggest that glycolaldehyde is a common hot-core tracer. In both hot-cores this line is blended with two methyl cyanide lines, as it is in G31, G24A1 and G24A2. We also acknowledge that the $46_{20,26}$–$46_{19,27}$ EE (E_u = 816 K, $S\mu^2$ = 2843 D^2) and $11_{11,1,1}$ – $10_{10,0,1}$AE (E_u = 63 K, $S\mu^2$ = 519 D^2) transitions of acetone may be contributing to the emission seen at this frequency. This is consistent with observations by Fuente et al. (2014), where they detect the $20_{2,18}$–$19_{3,17}$ transition of glycolaldehyde at 220 466 MHz, blended with acetone. In Section 5.3 we model both glycolaldehyde and acetone emission to explore this possibility. For the purposes of a chemical comparison between the hot cores in our sample, we have assumed that the line at 220 466 MHz is glycolaldehyde in the rest of the paper.

Figure 5 shows a map of the $18_{8,10}$–$17_{8,9}$E methyl formate emission (blue contours; line A, see Section 4.2), the $20_{2,18}$–$19_{3,17}$ glycolaldehyde emission (white contours) and

[2] For references see acknowledgements.

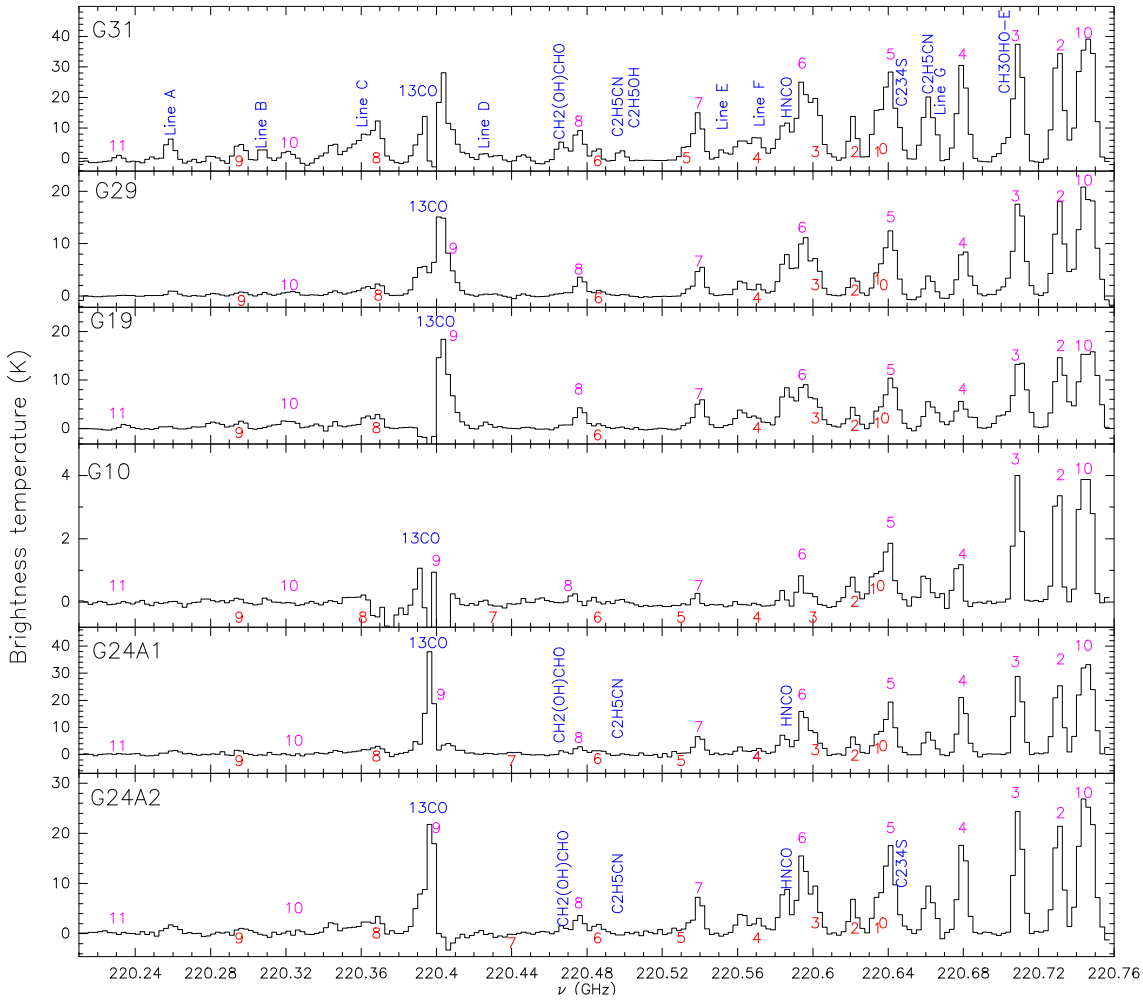

Figure 1. Spectra of the hot cores G31, G29, G19, G10, G24A1 and G24A2 observed with the PdBI (Beltrán et al. 2005, 2011), integrated over the 3σ contour level area. The species labelled are those that have already been identified in Beltrán et al. (2005) and Beltrán et al. (2011) as well as the 7 lines in G31 that were found but not identified by Beltrán et al. (2005). The numbers indicate the position of the CH_3CN (12_K–11_K) K-components in the upper part (in pink) of each spectra and of the CH_3 ^{13}CN (12_K–11_K) K-components in the lower part (in red).

the averaged emission of the K=0, 1, 2 (12–11) transitions of methyl cyanide emission (colour scale) in G31, G24A1, G24A2 and G29 (i.e. the four hot-cores for which the three molecular species have been detected). Methyl cyanide is a typical hot core tracer. For G24A1, G24A2, and G29 the three species seem to be tracing the same material and peak at roughly the same position towards the dust emission peak. On the other hand, in G31 glycolaldehyde peaks towards the centre of the core where the continuum source(s) is(are) embedded, whilst methyl formate and methyl cyanide show a different morphology. In particular, as reported by Beltrán et al. (2005) the methyl cyanide traces a toroidal structure with the strongest emission eastwards of the millimetre continuum emission peak, which is located towards the central dip. On the other hand, methyl formate does not show a toroidal morphology but peaks towards the eastern side of the core, at a position barely coincident with that of the methyl cyanide. (Beltrán et al. 2005) explained these apparent toroidal morphology as caused by the high optical depth and the existence of a temperature gradient in the core. In this scenario, glycolaldehyde appears to be less affected by excitation conditions, and a better tracer of the inner conditions of the hot-core closer to the embedded protostar(s). Methyl formate emission extends to 0.13 pc ($3\farcs5$) in G31 where the glycolaldehyde extends to 0.08 pc ($2''$). In G24, both methyl formate emission and glycolaldehyde emission extend to 0.11 pc ($3''$). In G29, both methyl formate emission and glycolaldehyde emission extend to 0.05 pc ($3''$).

4.2 New identifications

We now discuss some of the lines that were previously unidentified (see Fig. 1), namely A, B and E , for each source, and we compare the frequency, area of the Gaussian fitted, FWHM and peak brightness temperature in each hot core for each of the lines (see Table 4). It is clear from Fig. 1 that the spectra do vary among hot cores and that G31, the brightest hot core with $L_{bol} > 10^4 L_\odot$ (Beltrán et al. 2005)

Table 2. The observed frequency, velocity, area of Gaussian fit, FWHM, peak brightness temperature and the rms of the baseline for molecules previously detected in Beltrán et al. (2005) and confirmed in new cores in this work. Spectra are integrated over the 3σ contour level.

Molecule	Frequency† (MHz)	V_{LSR} (kms^{-1})	V_{peak}† (kms^{-1})	$\int T\,dv$ (Error) ($Kkms^{-1}$)	FWHM (kms^{-1})	T_B (K)	rms of baseline (K)
			G31.41+0.31				
CH_2OHCHO	220 466.35	96.8	93.6 (0.7)	40.5 (1.2)	6.8 (0.1)	5.6 (0.2)	0.3
HNCO	220 585.58	96.8	96.5 (1.0)	174.9 (22.5)	14.9 (2.4)	11.1 (0.9)	0.9
C_2H_5CN	220 661.45	96.8	96.3 (0.3)	203.5 (37.6)	9.7 (2.0)	19.7 (1.2)	0.3
			G29.96-0.02				
CH_2OHCHO	220 467.53	98.9	93.9 (3.4)	6.5 (1.1)	10.9 (2.1)	0.6 (0.1)	0.2
HNCO	220 585.88	98.9	98.0 (0.2)	85.6 (18.7)	10.5 (2.9)	7.7 (0.2)	0.3
C_2H_5CN	220 661.96	98.9	97.5 (0.4)	29.3 (9.2)	6.9 (2.5)	4.0 (0.1)	0.8
			G19.61-0.23				
CH_2OHCHO	220 467.67	41.6	36.4 (0.2)	5.8 (1.4)	6.9 (1.9)	0.8 (0.1)	0.2
HNCO	220 586.00	41.6	40.5 (0.2)	87.5 (41.4)	10.2 (5.5)	8.1 (0.3)	0.6
C_2H_5CN	220 662.77	41.6	39.1 (0.4)	61.0 (4.2)	10.8 (0.9)	5.3 (0.5)	0.9
			G24.78+0.08 A1				
CH_2OHCHO	220 467.22	110.8	106.5 (0.2)	8.0 (0.3)	4.3 (0.5)	1.8 (0.1)	0.2
HNCO	220 584.53	110.8	111.9 (0.2)	67.9 (16.3)	9.0 (2.5)	7.1 (0.3)	0.8
C_2H_5CN	220 661.67	110.8	110.0 (0.2)	68.5 (9.1)	7.8 (1.2)	8.2 (0.5)	1.1
			G24.78+0.08 A2				
CH_2OHCHO	220 466.94	110.8	106.8 (0.5)	10.3 (1.8)	5.8 (1.2)	1.7 (0.1)	0.3
HNCO	220 584.65	110.8	111.8 (0.1)	59.2 (35.6)	6.4 (4.1)	8.7 (1.5)	0.8
C_2H_5CN	220 661.67	110.8	110.0 (0.3)	83.0 (13.9)	8.4 (1.6)	9.3 (0.6)	1.0

† The small spread in frequency (0.2 – 2.4 MHz) between the rest frequency of the line and the observed frequency for each molecule in each hot core, is due to the difference between the V_{LSR} and the V_{peak} in each hot core. This difference is within the spectral resolution and V_{peak} error of the observations.

Table 3. Transitional information for the molecules previously detected in Beltrán et al. (2005) and confirmed in new cores in this work. All this transitional information was taken from the JPL spectral line catalog.

Molecule	Transition	Frequency (MHz)	E_u (K)	$S\mu^2$ (D^2)
CH_2OHCHO	20(2,18)–19(3,17)	220 463.88	120.05	89.74
HNCO	10(1,9)–9(1,8)	220 585.20	101.50	27.83
C_2H_5CN	25(2,24)–24(2,23)	220 660.92	143.02	367.60

is the most chemically-rich hot core in our sample. Lines C, D, F and G labelled in this figure could not be identified.

Line A is seen in four of the hot cores in our sample: G31, G29, G24A1 and G24A2 (Fig. 7). We have fitted a Gaussian profile to this line in each of the hot cores to determine their rest frequency, integrated intensity, FWHM, and brightness temperature (see Table 4). There is only a small spread in the observed rest frequency of this line from 220 258.240 MHz to 220 260.657 MHz, suggesting it is the same line in each hot core. Line A is brightest in G31, as expected. The FWHM range from 7.6 kms^{-1} in G29 to 11.1 kms^{-1} in G24A1.

The potential identities of line A consist of three lines of methyl formate ($HCOOCH_3$): $18_{8,10}$-$17_{8,9}$E, $24_{2,23}$-241, 24E, and $24_{2,23}$-$24_{0,24}$E; one line of methylene amidogen (H_2CN): $3_{2,1}$-$2_{2,0}$,F=11/2-9/2, (n=0-0)*; and one line of vinyl alcohol (C_2H_3OH): $11_{2,10}$-$11_{0,11}$. Methylene amidogen has previously been found in the cold core TMC-1 (Ohishi et al. 1994) and methyl formate and vinyl alcohol have previously been detected in hot cores (Fontani et al. 2007; Turner & Apponi 2001). Using criterion (iii) from Section 4 we can rule out methylene amidogen as there are several expected transitions in the frequency range of our observations that are not seen. Vinyl alcohol can also be ruled out because the $11_{2,10}$–$11_{0,11}$ transition has a low line intensity ($S\mu^2 = 0.03$), which leads to a column density of 2.7×10^{20} cm^{-2}, six orders of magnitude higher than the vinyl alcohol column density in Sagittarius B2(N) (Turner & Apponi 2001) and much larger than those of more commonly-observed molecules. We therefore identify line A with the $18_{8,10}$–$17_{8,9}$E transition of methyl formate, but the $24_{2,23}$–$24_{1,24}$E, and $24_{2,23}$–$24_{0,24}$E transitions also contribute to the line A emission. The $18_{8,10}$–$17_{8,9}$E transition of methyl formate is a high energy transition therefore it was not identified previously.

One notes however that, while all the expected transitions of methyl formate in our frequency range are detected in G31, this is not the case for the other hot cores (see Fig. 6). For example the 220 551.31 MHz $18_{6,12}$–$17_{6,11}$, vt=1

Table 4. The observed frequency, velocity, area of Gaussian fit, FWHM, peak brightness temperature and the rms of the baseline for lines A, B and E in each of the hot cores in our sample. Spectra are averaged over the 3σ contour level.

Object	Frequency† (MHz)	V_{LSR} (kms^{-1})	V_{peak} (kms^{-1})	$\int T\,dv$ (Error) ($K.kms^{-1}$)	FWHM (kms^{-1})	$T_{B,peak}$ (K)	rms of baseline (K)
			Line A				
G31	220 258.26	96.8	96.8	72.0 (1.8)	8.2 (0.3)	7.8 (0.2)	0.3
G29	220 260.05	98.9	96.2	8.3 (0.3)	7.6 (0.3)	1.02 (0.03)	0.2
G19				No detection rms = 0.2			
G10				No detection rms = 0.1			
G24A1	220 260.65	110.8	107.5	17.4 (2.9)	11.1 (2.2)	1.5 (0.2)	0.2
G24A2	220 259.28	110.8	109.2	19.4 (2.1)	10.3 (1.2)	1.8 (0.2)	0.3
			Line B				
G31	220 307.69	96.8	96.6	37.4 (2.0)	7.1 (0.5)	5.0 (0.3)	0.3
G29				No detection rms = 0.2			
G19				No detection rms = 0.2			
G24A1				No detection rms = 0.2			
G24A2				No detection rms = 0.3			
G10				No detection rms = 0.1			
			Line E				
G31	220 552.70	96.8	95.1	16.0 (4.5)	5.0 (2.8)	2.56 (0.9)	0.9
G29				No detection rms = 0.3			
G19				No detection rms = 0.6			
G10				No detection rms = 0.2			
G24A1				No detection rms = 0.8			
G2A2				No detection rms = 0.8			

† The small spread in frequency (0.2 – 2 MHz) between the rest frequency of the line and the observed frequency for each molecule in each hot core, is due to the difference between the V_{LSR} and the V_{peak} in each hot core. This difference is within the spectral resolution and V_{peak} error of the observations.

Table 5. The observed lines transitions, E_u, $S\mu^2$, and line list used for lines A, B and E.

Line	Molecule	Transition	Frequency (MHz)	E_u (K)	$S\mu^2$ D^2	Line list
Line A	$HCOOCH_3$ v=1	18(8,10) – 17(8,9)E	220 258.09	331	38.5	JPL
Line B	$HCOOCH_3$ v=1	18(10,9) – 17(10,8)E	220 307.38	354	33.2	JPL
Line E	$H^{13}COOCH_3$	18(6,12) – 17(6,11) ++v=1-1	220 551.30	313	43.9	TopModel

transition of methyl formate falls in a region of no detectable emission in the hot cores G29, G24A1 and G24A2. This may be an indication of temperature differences among hot cores as the intensity of methyl formate transitions is significantly temperature dependent.

Line B is only detected in G31 (see Fig. 8). Its potential line identities are three transitions of methylene amidogen (H_2CN) and one line of methyl formate ($18_{10,9}$–$17_{10,8}$E). Methylene amidogen can, again, be ruled out according to the (iii) criterion of Section 4, so the methyl formate $18_{10,9}$–$17_{10,8}$E transition is the best candidate for line B.

Line E is only detected in G31 (see Fig. 9). There are two potential line identities for line E, one line of a carbon-13 isotopologue of methyl formate ($H^{13}COOCH_3$), $18_{6,12}$–$17_{6,11}$, vt=1 and one line of propanal (CH_3CH_2CHO), $9_{4,5}$–$8_{2,6}$. There is only one bright line of propanal in the frequency range of these observations. This line falls in an area of little emission in the spectrum of G31 thereby ruling out propanal as a candidate. The $18_{6,12}$–$17_{6,11}$, vt=1 transition of methyl formate is therefore the best candidate for line E. The transitional information for these newly identified lines can be found in Table 5.

Clearly G31 is the most chemically rich object and in fact, of the three unidentified lines, B and E are only present in this source. In the next sections we derive column densities assuming Local Thermodynamic Equilibrium (LTE) and analyse our results through the use of a chemical model.

Table 6. Estimated rotational temperatures and column density of methyl formate calculated using the rotational temperature and using a source size measured in this work.

Object	Source size ($''$)	T_{rot} (K)	Column density (cm^{-2})
G31	3.5	169±39	4×10^{17}

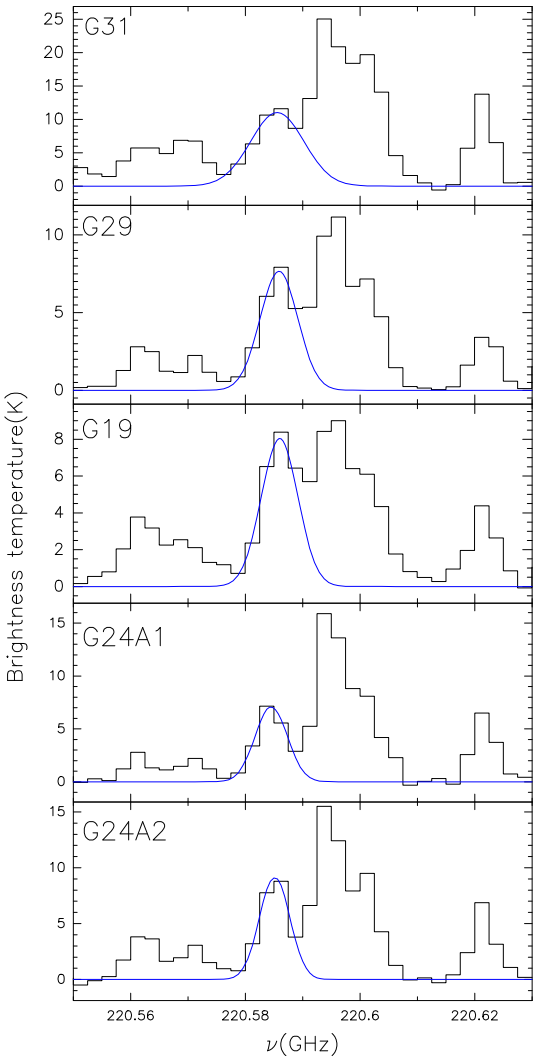

Figure 2. HNCO spectra with Gaussian fits, integrated over the 3σ contour level area toward G31, G29, G19, G24A1 and G24A2 as seen with the PdBI. This transition was previously detected in G31, G24A1 and G24A2 (Beltrán et al. 2005) and is detected in G19 and G29 in this work.

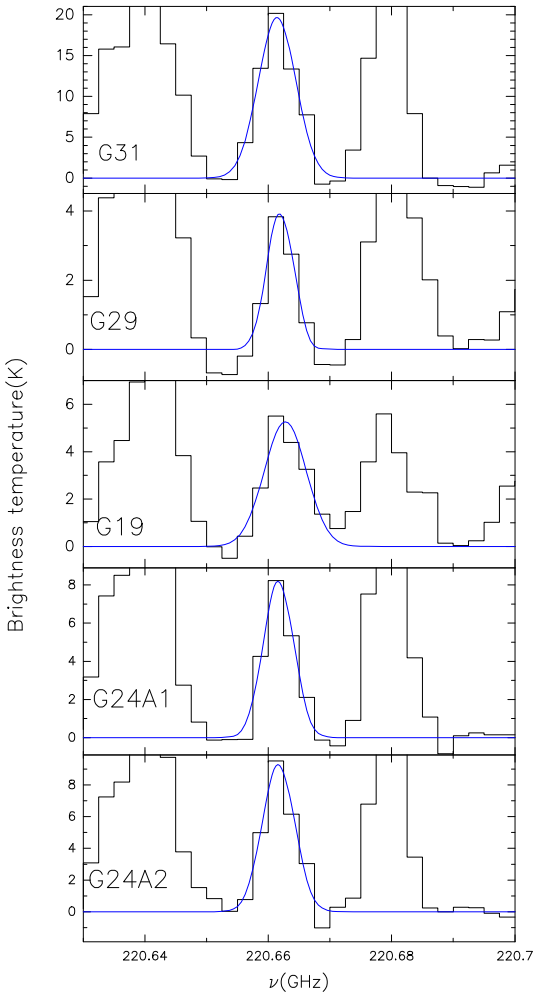

Figure 3. C_2H_5CN spectra with Gaussian fits, integrated over the 3σ contour level area toward G31, G29, G19, G24A1 and G24A2 as seen with the PdBI. This transition was previously detected in G31, G24A1 and G24A2 in Beltrán et al. (2005) and is detected in G19 and G29 in this work.

5 SPECTRAL LINE ANALYSIS

5.1 Estimates of excitation temperature

Methyl formate in G31 has been extensively studied and, aside from three newly-identified transitions, 26 transitions have been previously detected (Fontani et al. 2007) using the IRAM-30m. We therefore use the 29 lines of methyl formate in G31 to derive column densities and temperature estimates using a rotational diagram. We have accounted for the beam dilution of the IRAM-30m data using a source size of $3\farcs5$ as measured in Fig. 5. For the 3 newly-identified transitions we assume their emission fills the beam. The results can be seen in Fig. 10 and Table 6. The linear fits to the data in Fig. 10 have been calculated using a regression line, and the derived rotation temperatures agree very well with those of Fontani et al. (2007). The spread of data points from this regression line are within the error bars. The derived column density (Table 6) is in good agreement with the results of Fontani et al. (2007, $5.3 \times 10^{17}\,cm^{-2}$) and Isokoski et al. (2013, $1.7 \times 10^{17}\,cm^{-2}$) when assuming a source size of $3\farcs5$.

From the rotational diagram we find that, surprisingly,

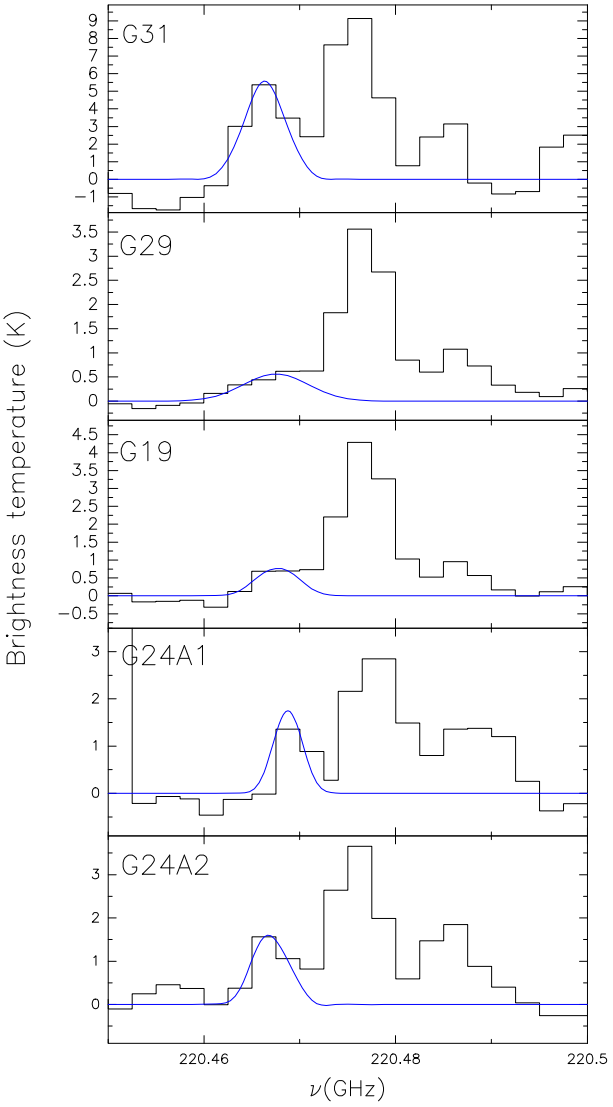

Figure 4. $CH_2(OH)CHO$ spectra with Gaussian fits, integrated over the 3σ contour level area toward G31, G29, G19, G24A1 and G24A2 as seen with the PdBI. This transition was previously detected in G31, G24A1 and G24A2 in Beltrán et al. (2005) and is detected in G19 and G29 in this work. In G29 it is only detected at a 3σ level. More transitions of glycolaldehyde are needed to confirm its presence in G29 and G19, and this line may be contaminated by the $46_{20,26}$-$46_{19,27}$ EE and $11_{11,1,1}$ – $10_{10,0,1}$AE transitions of acetone.

a single gas component with a temperature of ∼169 K can fit all 29 transitions. Note that line A and line B are vibrationally excited transitions of methyl formate and we would have expected them to trace a hotter region of gas.

5.2 Column density estimates

Table 7 lists calculated column densities for all identified molecules across our sample, derived using Equation 1 below, by assuming LTE at a constant temperature of 300 K, 225 K and 150 K, and optically thin emission (see Section 5.1 for a detailed discussion of the temperature of our hot cores).

$$N_u/g_u = \frac{N_{tot}}{Q(T_{rot})} e^{-E_u/T_{rot}} = \left(\frac{8\pi\nu^2 k \int T dv}{hc^3 A g_u}\right) \quad (1)$$

where g_u is the statistical weight of the level u, N_{tot} is the total column density of the molecule, $Q(T_{rot})$ is the rotational partition function, E_u is the energy of the upper energy level, k is the Boltzmann constant, ν is the frequency of the line transition, A is the Einstein coefficient of the transition, $\int T dv$ is the integrated line intensity. All column densities have been corrected for beam dilution by dividing the integrated line intensity by the beam dilution factor (Equation 2).

$$\eta_{BD} = \frac{\theta_S^2}{\theta_S^2 + \theta_B^2} \quad (2)$$

where θ_S is the source size and θ_B is the beam size.

For the IRAM-30m observations of G31 we use a beam size ranging from 10″– 24.″4. For the PdBI observations we assume the source fills the beam.

Table 7 shows that all our species peak in their density in G31. However, it is surprising that there is relatively little variation across the sample for HNCO and C_2H_5CN, both of which differ by a factor of 5 or less from source to source. HNCO densities are remarkably consistent throughout the sample. CH_3CN and $CH_2(OH)CHO$ show more variation, but if we exclude G31, then calculated column densities for the remaining objects in the sample again agree very well, to within a factor of ∼2.

5.3 Spectral Modelling

We have also analysed the observations using the spectral modelling software CASSIS and using the JPL Catalog. CASSIS has been developed by IRAP-UPS/CNRS (http://cassis.irap.omp.eu). We use the LTE (local thermodynamic equilibrium) analysis tool to determine the column densities and excitation temperatures, T_{ex}, required to reproduce the emission. The brightness temperature, T_b, of a given species is calculated by CASSIS according to:

$$T_b = T_C e^{-\tau} + (1 - e^{-\tau})(J_\nu(T_{ex}) - J_\nu(CMB)) \quad (3)$$

where T_C is the temperature of the continuum, τ is the opacity, CMB is the cosmic microwave background at 2.7 K, and $J_\nu(T) = h\nu/k)/(1 - e^{h\nu/kT} - 1)$ is the radiation temperature.

The input parameters for CASSIS are the column density, excitation temperature, source size, FWHM, and V_{LSR} for each species we observe. Values for the source size, FWHM, and V_{LSR} are taken from our observations. We vary the column densities and excitation temperatures for each species until a best fit is achieved. Further details of the CASSIS software and LTE analysis tool can found in the CASSIS documentation (http://cassis.irap.omp.eu/docs/RadiativeTransfer.pdf).

In particular, the spectral modelling focuses on the emission of CH_3CN, $HCOOCH_3$ and a possible contamination of the $CH_2(OH)CHO$ emission with $(CH_3)_2CO$, to test the validity of our line assignments. In this model we assume the gas is in LTE conditions at a temperature T_{ex}. A comparison of the column densities we derive from observation

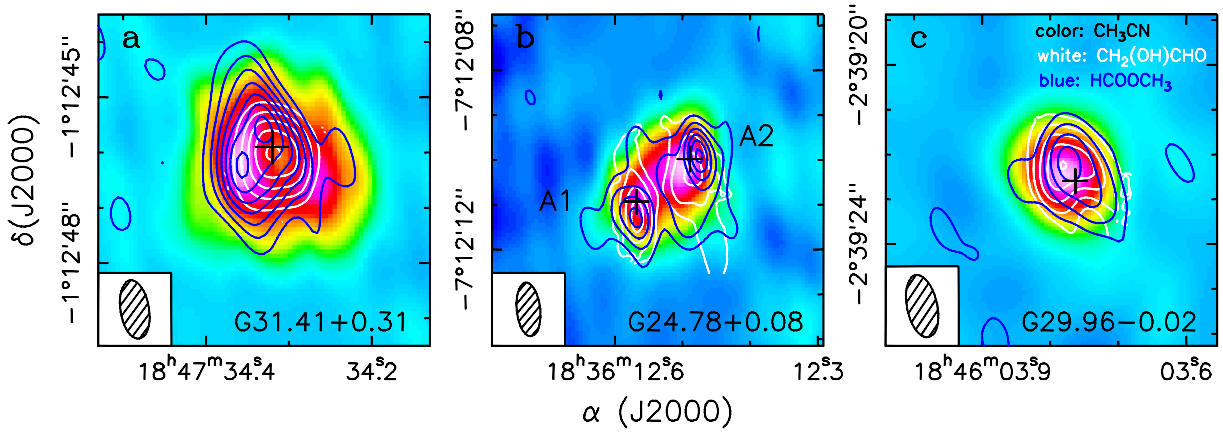

Figure 5. Spectral line map of the $18_{8,10}$-$17_{8,9}$E transition of methyl formate (blue contours), the $20_{2,18}$–$19_{3,17}$ transition of glycolaldehyde (white contours) and the averaged emission of the K=0, 1, 2 (12-11) transitions of methyl cyanide emission (colour scale) in G31, G29, G24A1 and G31. For the methyl formate in G31, the channels averaged were 91.7 – 101.9 kms^{-1}, with contour levels of 0.04 – 0.28 Jybeam^{-1}, in steps of 0.04 Jybeam^{-1}. In G24 the channels averaged for methyl formate were 102.4 – 112.6 kms^{-1}, with contour levels of 0.02 – 0.12 Jybeam^{-1}, in steps of 0.02 Jybeam^{-1}. In G29 the channels averaged for methyl formate were 91.1 – 101.3 kms^{-1}, with contour levels of 0.015 – 0.06 Jybeam^{-1}, in steps of 0.015 Jybeam^{-1}. For glycolaldehyde in G31, the channels averaged were 91.9 – 95.3 kms^{-1} with contour levels of 0.10 – 0.46 Jybeam^{-1}, in steps of 0.12 Jybeam^{-1}. In G24 the channels averaged for glycolaldehyde were 104.8 – 108.2 kms^{-1}, with contour levels of 0.04 – 0.12 Jybeam^{-1}, in steps of 0.04 Jybeam^{-1}. In G29 the channels averaged for glycolaldehyde were 92.2 – 95.6 kms^{-1}, with contour levels of 0.016 – 0.08 Jybeam^{-1}, in steps of 0.016 Jybeam^{-1}. For methyl cyanide the contour levels in G31 are 0.1–0.94 Jybeam^{-1} in steps of 0.12, in G24 they are 0.1 – 1.0 Jybeam^{-1} in steps of 0.18 Jybeam^{-1}, in G29 they are 0.09 – 1.14 Jybeam^{-1} in steps of 0.15 Jybeam^{-1}.

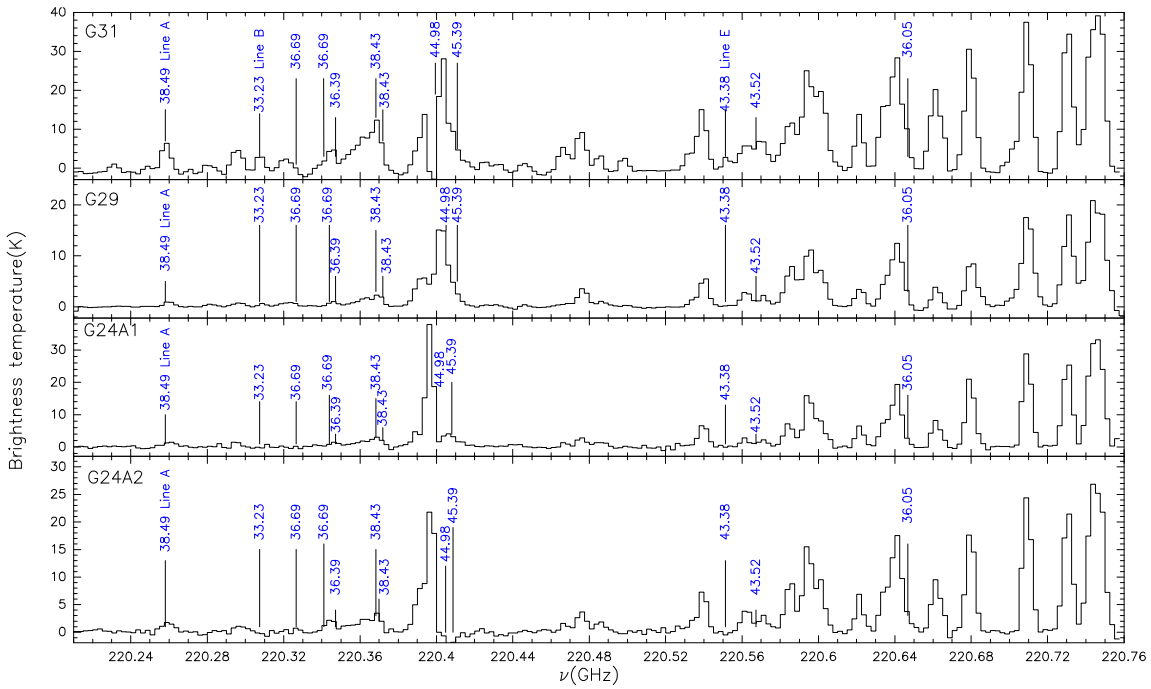

Figure 6. The expected bright emission of methyl formate transitions, that occur in the frequency range of our observations, plotted on the spectra of hot cores G31, G29, G24A1 and G24A2. The numbers on the plot represent the intensity (Sμ^2) of methyl formate transitions as determined by laboratory studies, in units of Debye^2.

and those we derive from spectral modelling can be found in Table 8.

Spectral models of CH_3CN emission, using only a single column density and excitation temperature, do not reproduce the observations accurately (Figure 11). We hypothesise that this 'poor' fit may be due to a combination of factors: (i) different transitions of CH_3CN may peak, or may be tracing, different temperatures and densities within our emission region, (ii) the emission we observe may not be in LTE, (iii) contributions due to blending, (iv) CH_3CN opacities are highly variable from the K=1 to the K=7 transitions, (v) the poor signal-noise ratio of the

Table 7. Column densities (cm^{-2}) of organic molecules in our sample, assuming LTE at 300 K, 225 K, and 150 K.

Object	HNCO	C_2H_5CN	CH_3CN^a	$CH_2(OH)CHO$	$HCOOCH_3$
			300 K		
G31	3×10^{16}	1×10^{16}	5×10^{16}	1×10^{17}††	1×10^{18}†††
G29	2×10^{16}	2×10^{15}	2×10^{16}	5×10^{15}	2×10^{16}
G19	1×10^{16}	3×10^{15}	1×10^{16}	3×10^{15}	...
G24A1	1×10^{16}	4×10^{15}	4×10^{16}	5×10^{15}	3×10^{16}
G24A2	2×10^{16}	5×10^{15}	3×10^{16}	6×10^{15}	4×10^{16}
			225 K		
G31	2×10^{16}	7×10^{15}	3×10^{16}	5×10^{16}††	8×10^{17}†††
G29	1×10^{16}	1×10^{15}	1×10^{16}	3×10^{15}	1×10^{16}
G19	1×10^{16}	2×10^{15}	8×10^{15}	2×10^{15}	...
G24A1	7×10^{15}	3×10^{15}	3×10^{16}	5×10^{15}	2×10^{16}
G24A2	8×10^{15}	3×10^{15}	2×10^{16}	6×10^{15}	2×10^{16}
			150 K		
G31	1×10^{16}	4×10^{15}	2×10^{16}	2×10^{16}††	4×10^{17}†††
G29	7×10^{15}	6×10^{14}	5×10^{15}	1×10^{15}	5×10^{15}
G19	5×10^{15}	1×10^{15}	4×10^{15}	8×10^{14}	...
G24A1	4×15^{15}	1×10^{15}	1×10^{16}	3×10^{15}	1×10^{16}
G24A2	5×10^{15}	2×10^{15}	1×10^{16}	3×10^{15}	1×10^{16}

[a] CH_3CN has been observed to be optically thick in all these objects (Beltrán et al. 2005, 2011) so the column densities have been derived using observations of $CH_3{}^{13}CN$.

†† The column density of glycolaldehyde for G31 has been obtained using the rotation diagram method by Beltrán et al. (2009)

††† The column density for this object was determined using the rotation diagram method using a source size of 3.″5, see 5.1.

high energy K-transitions. The best fit of all of the CH_3CN transitions is achieved at T_{ex} ranging from 410 – 450 K across our hot core sample. For $HCOOCH_3$ emission we have produced a spectral fit for the transition at 220.258 GHz (Figure 12) and the transition at 220.307 GHz. We are unable to model any isotopologues of methyl formate with CASSIS and have therefore omitted the transition at 220.553 GHz from our fit. In G31, where the observational column density was derived from multiple transitions of methyl formate, we find the required modelling column density to be the same as the observed value (4×10^{17} cm^{-2}). For the other hot cores we require a modelled column density a factor of 2 – 3 larger than the observed value. This is not surprising as the observed column density was derived from only one transition in these cores and therefore represents a lower estimate of the methyl formate column density in these objects. As we only have one confirmed methyl formate transition in several of our hot cores, it is difficult to accurately measure the T_{ex} required to reproduce these observations. We are confident from this modelling that we have correctly identified the $18_{8,10}$–$17_{8,9}$E and $18_{10,9}$–$17_{10,8}$E transitions of $HCOOCH_3$ in our hot core sample.

For $CH_2(OH)CHO$ emission we have produced a spectral fit for the transition at 220.466 GHz (Figure 13). For G31 the required column density to reproduce the spectra is similar to the observed value. For G29, G19, G24A1, and G24A2 the required modelling column densities are a factor of 1.5 – 3 larger than the observed values. This is likely due, again, to the observed column densities for these hot core being derived using only one $CH_2(OH)CHO$ transition, and therefore represents a lower estimate of the column densities in these hot cores.

We have also explored the possibility that this transition of glycolaldehyde is blended with the $46_{20,26}$–$46_{19,27}$ EE (E_u = 816 K, $S\mu^2$ = 2843 D^2) and the $11_{11,1,1}$ – $10_{10,0,1}$AE (E_u = 63 K, $S\mu^2$ = 519 D^2) transitions of acetone. We find for column densities and excitation temperatures of acetone which produce enough emission to explain the line at 220 466 MHz, we overproduce emission at 220 368 MHz. It is possible that both acetone and glycolaldehyde could be present in the hot cores in our sample, however, the contribution of acetone to the line seen at 220 466 MHz is not significant (<7%). More observations are needed to confirm the presence of both glycolaldehyde and acetone in these hot cores.

Chemical differentiation in hot cores has been observed before (Mookerjea et al. 2007; Garay & Lizano 1999) and attributed to either differences in their host star mass and/or differences in ages. Results of chemical models in the past have suggested that determining abundance ratios of typical hot core tracers (e.g. CH_3CN) as well as sulphur-bearing species could serve as indicators of both mass and age (Hatchell et al. 1998; Viti et al. 2001; Buckle & Fuller 2003; Viti et al. 2004). However much care has to be taken due to the fact that most species do not necessarily trace the very inner part of the core and their emission region probably spans a range of densities and temperatures that make the interpretation difficult (Wakelam et al. 2004). The com-

Table 8. Spectral modelling column densities and excitation temperatures of methyl cyanide, methyl formate and glycolaldehyde.

Hot Core	T_{ex} (K)	Modelled column density (cm^{-2})	Observed at column density (cm^{-2})
		CH_3CN	
G31	450	9×10^{15}	5×10^{16} (300 K)
G29	410	5×10^{15}	2×10^{16} (300 K)
G19	450	4×10^{15}	1×10^{16} (300 K)
G24a1	310	4×10^{15}	4×10^{16} (300 K)
G24a2	450	6×10^{15}	3×10^{16} (300 K)
		$HCOOCH_3$	
G31	130	4×10^{17}	4×10^{17} (150 K)
G29	300	5×10^{16}	2×10^{16} (300 K)
G24A1	300	9×10^{16}	3×10^{16} (300 K)
G24A2	300	1×10^{17}	4×10^{16} (300 K)
		$CH_2(OH)CHO$	
G31	130	3×10^{16}	2×10^{16} (150 K)
G29	300	8×10^{15}	5×10^{15} (300 K)
G19	300	9×10^{15}	3×10^{15}(300 K)
G24A1	300	1×10^{16}	5×10^{15} (300 K)
G24A2	300	1×10^{16}	6×10^{15} (300 K)

plex species we have been discussing in this paper, on the other hand, may provide us with a better choice of age/mass discrimination as they all seem to trace a more compact region than the more widely-observed species such as CH_3OH and CH_3CN. In the next section we make use of a chemical model, UCL_CHEM (Viti et al. 2004) to simulate the formation and evolution of hot cores and see if the differences in ratios of the species listed in Table 7, between G31 and the rest of the cores, can shed some light on the masses and ages of our sources.

6 CHEMICAL MODELLING

UCL_CHEM (Viti et al. 2004) is a two-phase time-dependent model which follows the collapse of a prestellar core (Phase I), followed by the subsequent warming and evaporation of grain mantles (Phase II). Phase I starts from the number density of a diffuse cloud ($10^2\,cm^{-3}$) and allows a free-fall collapse to take place until a final density (which varies between $10^{6-8}\,cm^{-3}$) is reached. This occurs isothermally at a temperature of 10 K. During the collapse, atoms and molecules collide with, and freeze on to, grain surfaces. The depletion efficiency is determined by the fraction of the gas-phase material that is frozen on to the grains (Rawlings et al. 1992). This fraction is arrived at by adjusting the grain surface area per unit volume, and assuming a sticking probability of unity for all species. The fraction of material on grains is then dependent on the product of the sticking probability and the amount of cross-section provided per unit volume by the adopted grain size distribution. Grains are considered to be spheres. We assume that hydrogenation occurs rapidly on the grain surfaces, so that, for example, some percentage of carbon atoms accreting will rapidly become frozen out methane (CH_4) etc. In Phase II we increase the dust and gas temperature up to 300 K, to simulate the presence of a nearby infrared source in the core. As the temperature increases, mantle species desorb in various temperature bands (see Collings et al. (2004)). UCL_CHEM treatment of the temperature and of the ice sublimation is as in (Viti et al. 2004), where details of how the temperature increases with time leading to the subsequent time dependent sublimation of the ice mantles can be found.

Initial atomic abundances are taken from Sofia & Meyer (2001), as in Viti et al. (2004). For the gas-phase chemistry, reaction rate coefficients are taken from the UMIST database (Woodall et al. 2007). Some coefficients have been updated with those from the KIDA database (Wakelam et al. 2009). Our database also includes some simple grain-surface reactions (mainly hydrogenation) as in Viti et al. (2004) as well as selected routes for grain-surface formation of glycolaldehyde as in Woods et al. (2012) and methyl formate as in Occhiogrosso et al. (2011). In Phase I non-thermal desorption is considered as in Roberts et al. (2007).

We investigate how varying key model parameters, such as the final collapse density, lifetime of the cold phase, the type of evaporation, and the efficiency of the freeze-out of species (measured as a percentage of the total CO in the solid phase) affect the abundances of methyl cyanide, methyl formate, glycolaldehyde, ethyl cyanide and isocyanic acid during the hot core evolution. We have modelled hot cores with final densities of $10^6\,cm^{-3}$, $10^7\,cm^{-3}$ and $10^8\,cm^{-3}$. We also vary the efficiency of the freeze-out of species from 14%–100%. Since the period in which the grains are warmed from very low temperatures to the temperatures observed in typical hot cores is determined by the time taken for a prestellar core to evolve towards the Main Sequence, and hence by its mass (Viti & Williams 1999) we have explored the effect of new-born stars with different masses (15 $M_\odot$ and 25 $M_\odot$), corresponding to contraction times of 118 000 yr and 70 000 yr respectively – see Bernasconi & Maeder (1996).

In the following section we explore the sensitivity of

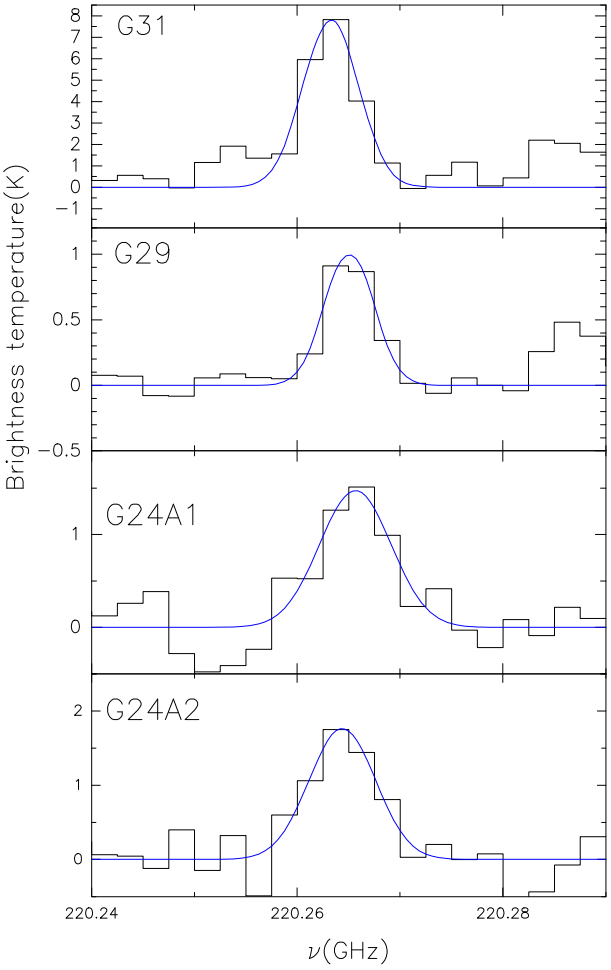

Figure 7. Spectra of Line A with Gaussian fits, integrated over the 3σ contour level area toward G31, G29, G24A1 and G24A2 as seen with the PdBI. This transition was previously detected in G31 but was not identified, in Beltrán et al. (2005), and is also detected in G24A1, G24A2 and G29 in this work.

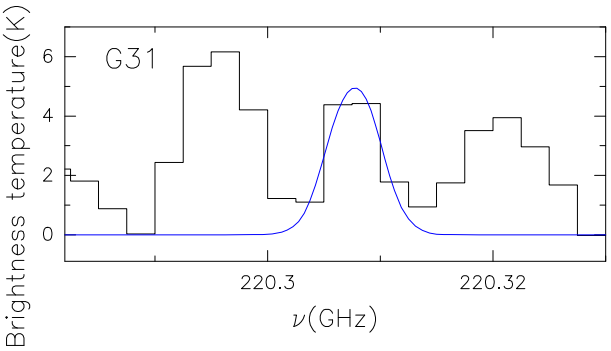

Figure 8. Spectra of Line B with a Gaussian fit, integrated over the 3σ contour level area toward G31 as seen with the PdBI. This transition was previously detected in G31 but was not identified in Beltrán et al. (2005).

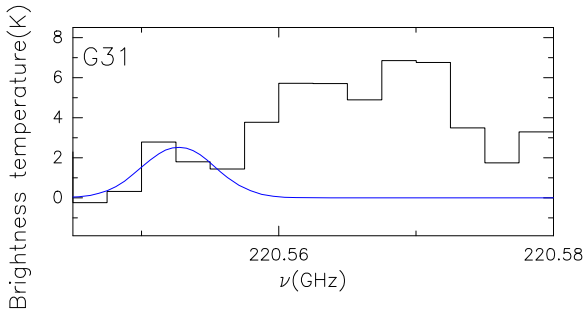

Figure 9. Spectra of Line E with a Gaussian fit, integrated over the 3σ contour level area toward G31 as seen with the PdBI. This transition was previously detected in G31 but was not identified in Beltrán et al. (2005).

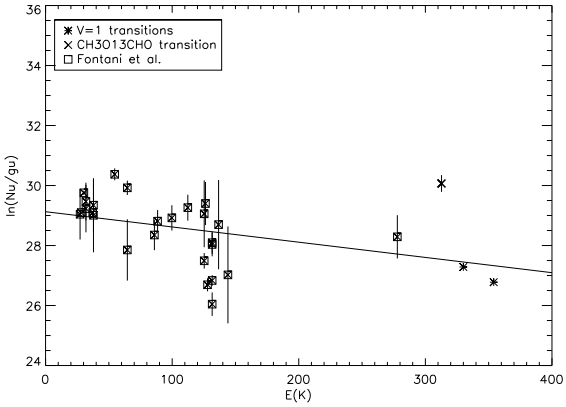

Figure 10. A rotation diagram of methyl formate transitions in G31, extending the work of Fontani et al. (2007) to higher excitation temperatures. A $^{12}C/^{13}C$ ratio of 41 was calculated according to Wilson & Rood (1994) using the Galactic Coordinates of G31 and a source size of 3.″5 was assumed based on the observed distribution seen in Fig. 5. Errors for the v=1 excited transitions are so small (<0.02) that they do not appear on this diagram.

the aforementioned species to changes in the physical and chemical parameters described above, before comparing our theoretical models with observations. Plots 14–16 show gas-phase abundances in Phase II of the model, for ease of comparison to observationally-derived results.

6.1 Sensitivity to stellar masses

Figure 14 shows an example of two models, each with a final density at the end of Phase I of 10^7 cm^{-2} and a freeze-out percentage of ≈60% in the solid phase, differing in the final mass of the star in Phase II. At ≈ $10^{4.5}$ years the sudden jump in abundance of methyl formate and ethyl cyanide is due to the evaporation of these species from the grain mantle surface. At late times varying the final mass of the star does not seem to affect the fractional abundances of the complex species we consider; however, as expected (see Viti et al. 2004), a higher mass implies an earlier icy mantle evaporation. In general a very low abundance of COMs implies a young age with the exception of methyl cyanide (but see Sect. 6.3) whose abundance is high regardless of the age

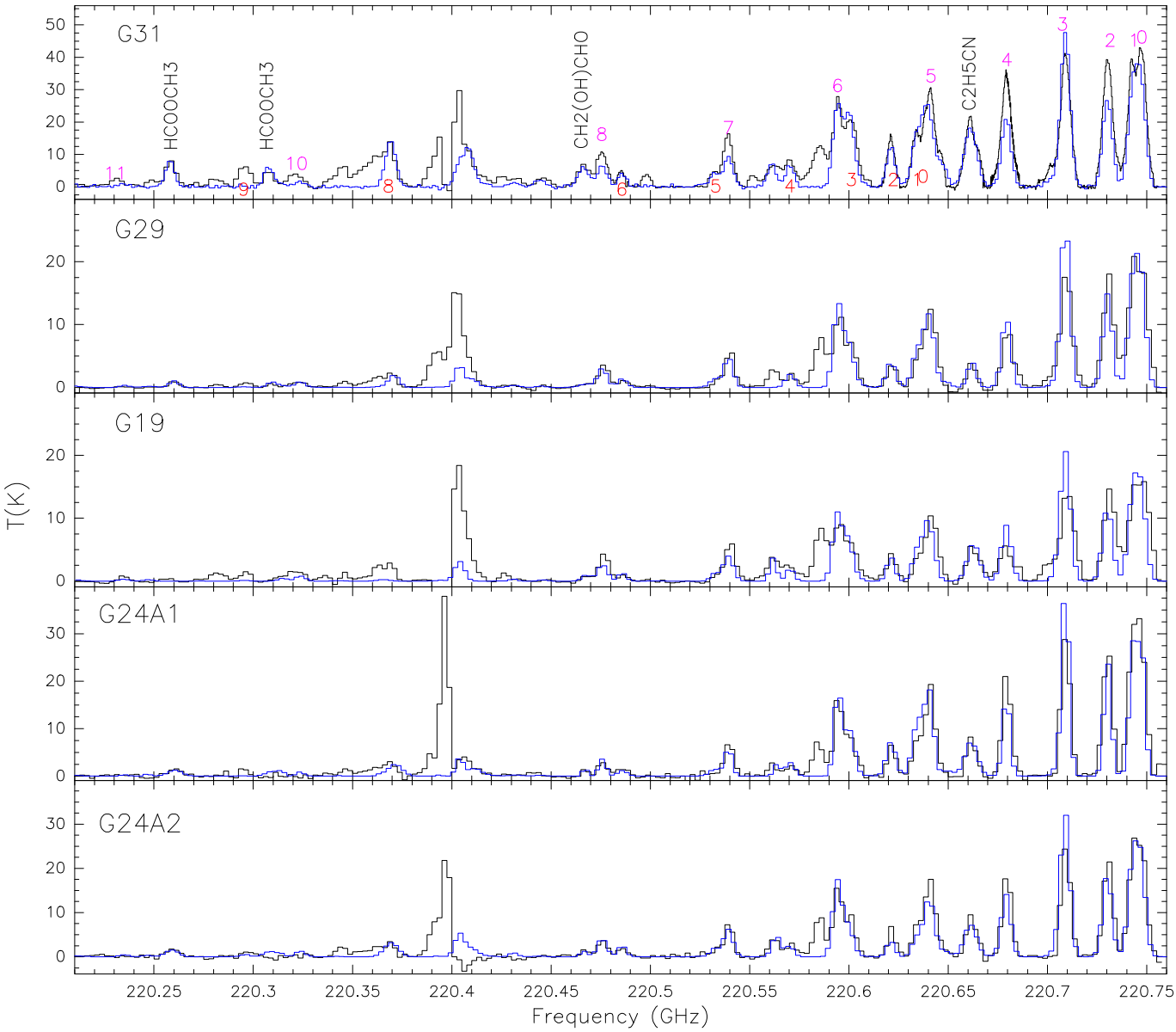

Figure 11. CASSIS modelling (blue line) of methyl formate ($HCOOCH_3$), glycolaldehyde ($CH_2(OH)CHO$), methyl cyanide (CH_3CN), and ethyl cyanide (C_2H_5CN) overlaid on the PdBI observations (black line). We label the molecules detected in this work in the G31 panel. The numbers indicate the position of the CH_3CN (12_K–11_K) K-components in the upper part (in pink) of each spectra and of the CH_3 ^{13}CN (12_K–11_K) K-components in the lower part (in red). We have excluded the ^{13}CO line from these models since there is an issue of missing line flux in several of the hot core observations.

of the core; hence, a core where this species is the *only* abundant complex molecule may be a very young core. The theoretical low fractional abundances before evaporation translate into column densities of the order of $<10^{10}\,cm^{-2}$, much lower than the lowest observed values for our sample.

6.2 Sensitivity to the icy mantle composition

Figure 15 is a plot of the fractional abundances of selected species at 10^5 yr after Phase II starts, as a function of the percentage of CO left in the solid phase at the end of Phase I. Note that after few thousand years from the beginning of Phase II CO will have completely evaporated back into the gas phase so the percentage on the x-axis is *not* an indication of the final gas CO abundance. In the figure, we present models which use two different values of the reaction rate coefficient for the formation of glycolaldehyde. This is due to the uncertainties in the value of this quantity (see Woods et al. (2012)). Based on the sensitivity analysis of (Woods et al. 2012), we only consider one formation route for glycolaldehyde for simplicity: g-CH_3OH + g-HCO → g-$CH_2(OH)CHO$, where g- refers to a species which is frozen onto the grain surface. As expected, the abundance of most complex species increases with an increase in freeze-out efficiency (corresponding to a decrease in percentage of CO

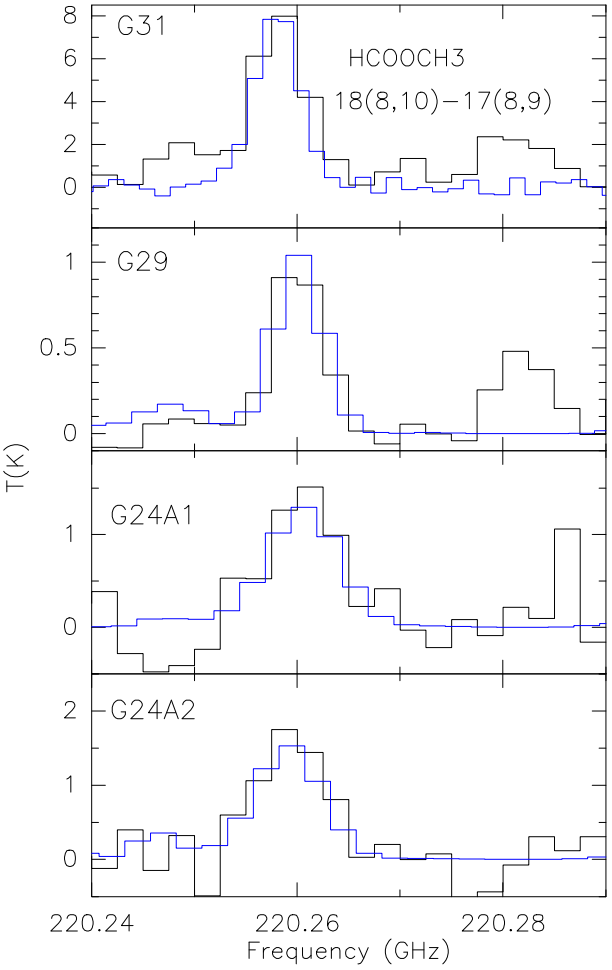

Figure 12. Models of the $18_{8,10}$–$17_{8,9}$E transition of $HCOOCH_3$ using CASSIS (blue line) overlayed on the PdBI observations (black line).

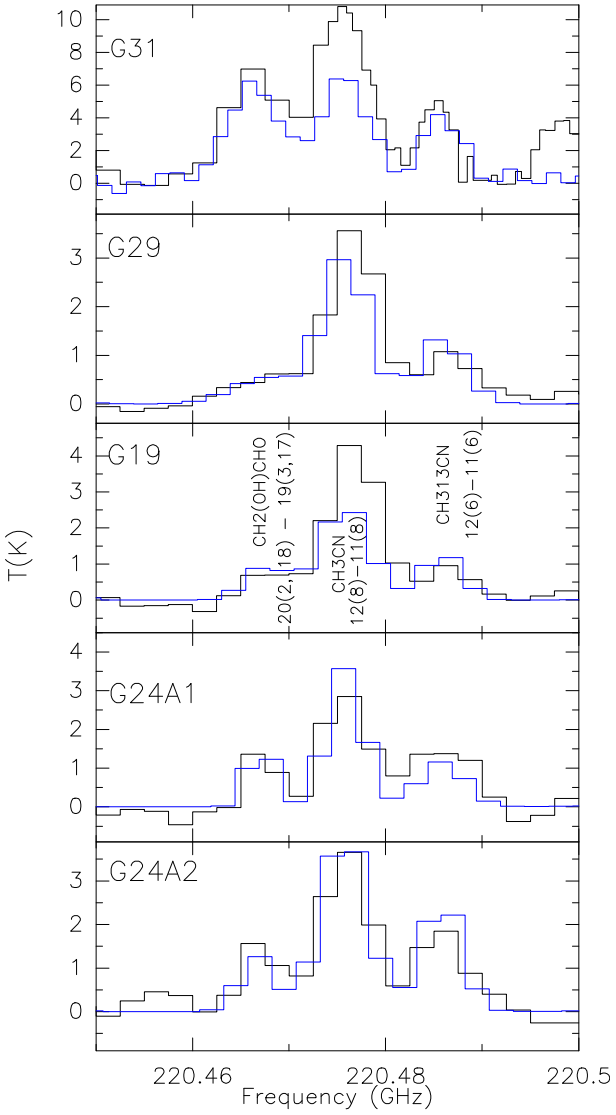

Figure 13. $CH_2(OH)CHO$ spectra with CASSIS models (blue line) overlaid on the PdBI observations (black line). From left to right: the $20_{2,18}$-$19_{3,17}$ transition of glycolaldehyde, the 12(8)-11(8) transition of CH_3CN, and the 12(6)-11(6) transition of $CH_3{}^{13}CN$.

in the gas phase). However it is interesting to note that ethyl cyanide seems to decrease at a very high freeze out efficiency while the abundance of methyl cyanide is more or less constant. The main route of formation for ethyl cyanide is via hydrogenation of HC_3N on the grains so in principle its abundance should increase with the efficiency of freeze-out. However, as HC_3N is efficiently formed in the gas phase via reactions involving H_2O, HCN and other hydrocarbons, when freeze-out is very efficient the reactants are depleted from gas deposited on the grains at a higher efficiency than that of the reactions forming HC_3N.

6.3 Sensitivity to the gas density

Figure 16 shows the abundance of our selected molecules as a function of time for three different final densities. The fractional abundance of most species increases with density when going from 10^6 to $10^7\,cm^{-3}$ although the increase is less pronounced at high densities. An interesting effect of increasing densities is observed with methyl cyanide whose abundance before thermal evaporation is still high at the lowest density while it drops considerably at high densities: we interpret this as a direct effect of freeze-out, which is directly proportional to collisional frequency of the parent species forming CH_3CN during phase I. Finally we note that, at a late stage of the evolution of the core, the ratio of the selected COMs varies as a function of density: for example, at lower densities CH_3CN is always higher than the other organic molecules while already at $10^7\,cm^{-3}$ CH_3CN/C_2H_5CN is $\sim$1 and at higher densities, $<$1. Similar considerations can be made about other species, making the ratios of our selected COMs ideal tracers of densities for evolved hot cores.

6.4 Comparison with observations

Table 7 shows that the differences in column densities among cores, for most species, are seldom larger than one order of magnitude; considering the uncertainties in model parameters as well as formation and destruction rates for COMs, it is therefore not possible, at present, to use chemical models

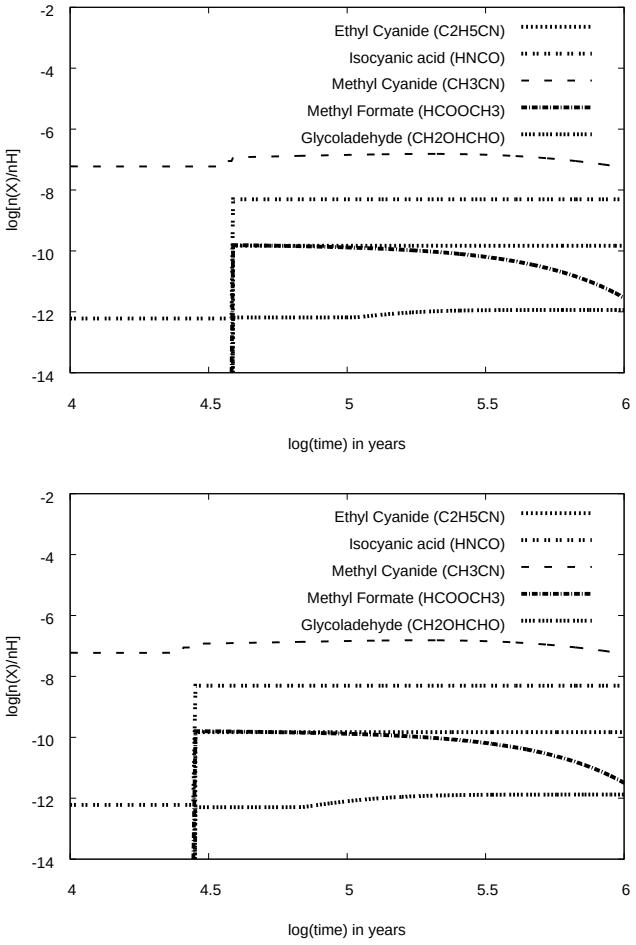

Figure 14. Gas phase fractional abundances of selected species as a function of time for a $15\,M_\odot$ (top) and a $25\,M_\odot$ star (bottom), both with a final gas density after Phase II of 10^7 cm^{-3}. At $\approx 10^{4.5}$ years the sudden jump in abundance of methyl formate and ethyl cyanide is due to the evaporation of these species from the grains mantle surface.

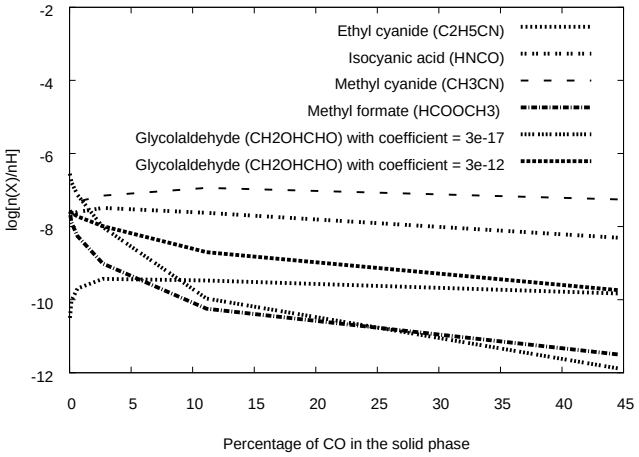

Figure 15. Fractional abundances of selected species at 10^6 yr after the 'switch on' of the star as a function of the percentage of CO left in the solid phase at the end of Phase I, for a $25\,M_\odot$ star with a final gas density after phase I of 10^7 cm^{-3}.

to infer the age or the mass of each individual core. Nevertheless, we do attempt a qualitative comparison with observations by estimating theoretical column densities from our models. We derive the theoretical column density N by using the approximate formula below:

$$N = X \times A_{\rm V} \times {\rm N}_{H2}, \quad (4)$$

where X is the fractional abundance from our models and N_{H2} is the column density of H_2 that provides 1 mag of extinction (Bohlin et al. 1978), which is 1.6×10^{21} cm^{-2}. For $A_{\rm V}$ we adopt a typical hot core visual extinction of 600 mags (noting that the column density simply scales linearly with extinction and that the fractional abundances calculated from the models are insensitive to visual extinctions above a critical value of ∼10 mags, when photons do not penetrate any further).

The first general conclusion we can draw by comparing Table 7 with our models (see Figs. 13, 15 and 16) is that all cores are evolved enough that all the mantles have evaporated. From our models this means that they are at least 20,000 yr old cores (this estimate increases with decreasing mass).

We find that most models match the theoretical abundance of HNCO quite well: the theoretical column densities vary between 8×10^{15} and 3×10^{16} cm^{-2} where the upper values coincide with models with a high density and freeze out (as expected since HNCO forms mainly on the grains). HNCO seems to be fairly constant among cores and its observed column densities are closer to the upper theoretical values; hence the only tentative conclusion we can derive here is that the density of the observed cores is $>10^6$ cm^{-3}, possibly as high as 10^8 cm^{-3}; this is consistent with the emission of COMs being so compact that they trace the gas closer to the protostar.

C_2H_5CN is, on the other hand, always under abundant in our models although, again, it is highest in models where the density and freeze out are high. We note that, among the cores, the highest value for this species is found in G31, implying a higher density for this core.

CH_3CN shows a larger variation in observed column densities, from 10^{16} cm^{-2} in G19 to 5×10^{16} in G31. A similar range is found in our models as a function, again, of density, although interestingly not of freeze out (see Fig. 14). Again we conclude that G31 is the densest core, with n_H close to 10^8 cm^{-3}.

The observed CH_2(OH)CHO column density is similar among all cores but G31, where it is two orders of magnitude higher than in the other objects. It is interesting to note that we can match its column density with models of gas densities of the order of 10^8 cm^{-3} for G31 and 10^6–10^7 cm^{-3} for the rest of the cores, again supporting the conclusion that G31 has a higher gas densities than the rest of the objects in our sample. We note that only models where we use a high rate coefficient for the formation of glycolaldehyde are able to reproduce the observations, in agreement with the findings of (Woods et al. 2012).

Finally, $HCOOCH_3$ shows the same behaviour as glycolaldehyde in that it is higher by at least one order of magnitude in G31 compared to the rest of the sample where it is

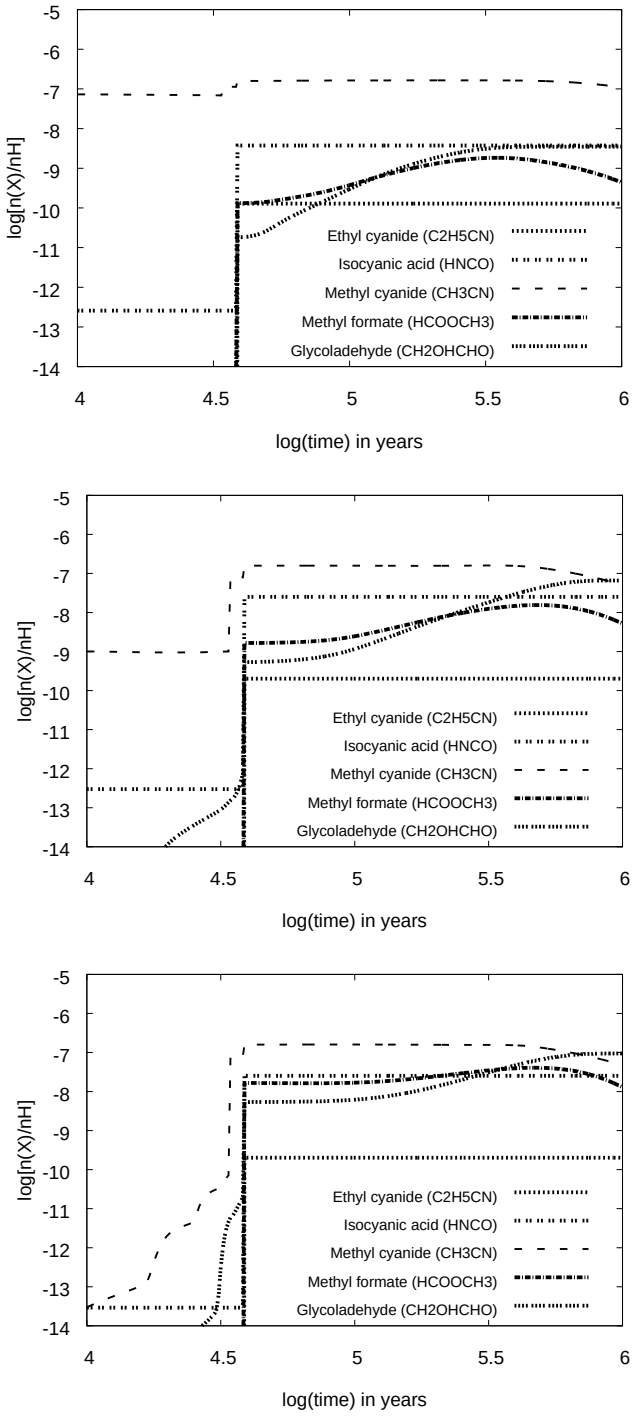

Figure 16. The gas phase abundance of isocyanic acid, ethyl cyanide, methyl cyanide, methyl formate, and glycolaldehyde as a function of time for the percentage of CO left in the solid phase of 100% , a mass of 15 $M_{\odot}$, equivalent to a contraction time of 115 000 yr, with step evaporation of the icy mantles. The top panel corresponds to a final density after phase I of 10^6 cm^{-3}. The middle panel corresponds to a final density after phase I of 10^7 cm^{-3}. The bottom panel corresponds to a final density after phase I of 10^8 cm^{-3}.

more or less constant at 10^{16} cm^{-2}. In our models, we reach a column density of 10^{16} cm^{-2} at gas densities of 10^7 cm^{-3}; interestingly an increase to 10^8 cm^{-3} only yields an increase in methyl formate by a factor of few and only for a relatively short period of time, since this species seems to decline in abundance after 5×10^5 yrs. However we point out that the column density for G31 was derived using a temperature derived from a rotational diagram, while for all the other cores a simple LTE calculation at 300K was performed. In fact, in general, LTE calculations at lower temperature would yield a lower column densities.

7 CONCLUSIONS

We have analysed IRAM PdBI data, in the frequency range 220 209.95 MHz to 220 759.69 MHz, towards six hot cores: G31.41+0.31, G29.96-0.02, G19.61-0.23, G10.62-0.38, G24.78+0.08A1 and G24.78+0.08A2. The aim was to identify seven lines that were unidentified by Beltrán et al. (2005) in G31 and look for their presence in the other five hot cores, as well as identify other complex molecules that were identified by Beltrán et al. (2005) in G31 and G24 but not in G29, G19 and G10.

We have identified three new transitions of methyl formate (HCOOCH3) in G31, two of which are vibrationally excited lines. A rotation diagram analysis of these lines combined with those in (Fontani et al. 2007) yields a column density for methyl formate of 4×10^{17} cm^{-2}. This is at least two orders of magnitude larger than the column densities in the other hot cores in our sample. We have also found a single temperature component of ∼170 K (using a source size of 3.″5) that fits these transitions, although the vibrationally-excited transitions we have found and our very large column densities would suggest that methyl formate may trace multiple temperature components of G31. This may also be true of the hot cores in G29 and G24. The spatial distribution of methyl formate does indicate that it traces the dense and compact parts of hot cores. Comparatively methyl formate traces a region slightly more compact than that of methyl cyanide but glycolaldehyde emission still remains the most compact to date. At this stage we can not conclude whether the fact that methyl formate is more extended than glycolaldehyde is a question of excitation or chemistry. We do find, however, that in G29 methyl formate and glycolaldehyde are tracing a an emission region of 0.05 pc which is comparable to the compact emission of glycolaldehyde in G31 (0.08pc). In G24 methyl formate and glycolaldehyde both trace a region comparable in size to the region traced by methyl formate in G31. In our models we do not find a density where there is more methyl formate than glycolaldehyde which would suggest that glycolaldehyde forms in a smaller denser region. We note, however our glycolaldehyde network of reactions is far from complete and it is therefore likely that we form too much glycolaldehyde in our model.

In this work we postulate that we have found the $20_{2,18}$-$19_{3,17}$ transition of glycolaldehyde in two more hot cores bringing the total number of detections in high mass star forming regions, outside the Galactic Centre, to five

hot cores. This emission whilst being far more compact in G31, is of comparable compactness to methyl formate in G24A1, G24A2 and G29. We have spectrally modelled our emission to explore the possible contamination of this transition with the $46_{20,26}$–$46_{19,27}$ EE and $11_{11,1,1}$ – $10_{10,0,1}$AE transitions of acetone. We find that any contribution of acetone emission to the lie seen at 220 466 MHz is not significant. More observations are needed to confirm the presence of glycolaldehyde in these hot cores. Our other complex molecule detections in our sample highlight chemical homogeneity among G29, G19, G24A1 and G24A2, not only in terms of presence or absence of certain transitions but also when comparing column densities. G31, however, is the most chemically rich object and the significantly different column densities we find in this core and the variety of transitions seen may suggest that it represents a different evolutionary stage to the other hot cores in our sample, or it may surround a star with a higher mass.

We have also undertaken a comparison between observations and a chemical model, UCL CHEM, to interpret the molecular inventory of the six cores and qualitatively characterise each core and its evolutionary stage. We note that of the species we are modelling, only methyl formate and methyl cyanide have been extensively studied in the laboratory (Modica & Palumbo 2010; Bennett & Kaiser 2007; Khlifi et al. 1996; Defrees et al. 1985; Huntress & Mitchell 1979). The other complex molecules are little-known and it is very likely that our models are missing routes of formation and destruction for these species. Moreover, we note that the LTE calculations shown in Table 6 were for a temperature of 300K; a lower temperature would in general yield a lower column density. The uncertainties related to the size of the emission region and temperatures, together with the incompleteness of the chemical networks for COMs makes a more quantitative comparison with chemical modelling inappropriate.

In conclusion, a qualitative comparison between our modelling and observations seem to consistently yield a higher density for G31 than the other objects in our sample, a result consistent with the fact that most lines are indeed the brightest in G31. We can also safely conclude that our sample only contains evolved hot cores, with an age of at least 20,000 years. We are unable to constrain the mass of each core; this information would have led to a better constraint for the age of each core.

ACKNOWLEDGMENTS

This research is supported by an STFC PhD studentship and the LASSIE Initial Training Network under the European Communitys Seventh Framework Programme FP7/2007-2013 under grant agreement No. 238258. Funding for this work was also provided by the Leverhulme Trust.

Data was reduced using the Gildas software package [3]. Spectral line data were taken from the Spectral Line Atlas of Interstellar Molecules (SLAIM; Available at `http://www.splatalogue.net`. F. J. Lovas, private communication, Remijan et al. 2007), the JPL Spectral Line Catalog (Pickett et al. 1998), the Cologne Database for Molecular Spectroscopy (Müller et al. 2005) and the Lovas/NIST database (Lovas & Dragoset 2004).

[3] http://www.iram.fr/IRAMFR/GILDAS

REFERENCES

Argon A. L., Reid M. J., Menten K. M., 2000, Astrophysical Journal, Supplement, 129, 159
Beltrán M. T., Cesaroni R., Codella C., Testi L., Furuya R. S., Olmi L., 2006, Nature, 443, 427
Beltrán M. T., Cesaroni R., Moscadelli L., Codella C., 2007, Astronomy and Astrophysics, 471, L13
Beltrán M. T., Cesaroni R., Neri R., Codella C., 2011, Astronomy and Astrophysics, 525, A151
Beltrán M. T., Cesaroni R., Neri R., Codella C., Furuya R. S., Testi L., Olmi L., 2004, Astrophysical Journal, Letters, 601, L187
Beltrán M. T., Cesaroni R., Neri R., Codella C., Furuya R. S., Testi L., Olmi L., 2005, Astronomy and Astrophysics, 435, 901
Beltrán M. T., Codella C., Viti S., Neri R., Cesaroni R., 2009, Astrophysical Journal, Letters, 690, L93
Beltràn M. T., Codella C., Viti S., Neri R., Cesaroni R., 2010, Highlights of Astronomy, 15, 701
Beltrán M. T., Estalella R., Anglada G., Rodríguez L. F., Torrelles J. M., 2001, Astronomical Journal, 121, 1556
Benjamin R. A., 2003, in Bailes M., Nice D. J., Thorsett S. E., eds, Radio Pulsars Vol. 302 of Astronomical Society of the Pacific Conference Series, The Distribution of the Warm Ionized Medium in the Galaxy. p. 271
Bennett C. J., Kaiser R. I., 2007, Astrophysical Journal, 661, 899
Bernasconi P. A., Maeder A., 1996, Astronomy and Astrophysics, 307, 829
Beuther H., Zhang Q., Bergin E. A., Sridharan T. K., Hunter T. R., Leurini S., 2007, Astronomy and Astrophysics, 468, 1045
Blum R. D., Damineli A., Conti P. S., 2001, Astronomical Journal, 121, 3149
Bohlin R. C., Savage B. D., Drake J. F., 1978, Astrophysical Journal, 224, 132
Bonnell I. A., Bate M. R., Zinnecker H., 1998, Monthly Notices of the RAS, 298, 93
Buckle J. V., Fuller G. A., 2003, Astronomy and Astrophysics, 399, 567
Cesaroni R., Beltrán M. T., Zhang Q., Beuther H., Fallscheer C., 2011, Astronomy and Astrophysics, 533, A73
Cesaroni R., Churchwell E., Hofner P., Walmsley C. M., Kurtz S., 1994, Astronomy and Astrophysics, 288, 903
Cesaroni R., Codella C., Furuya R. S., Testi L., 2003, Astronomy and Astrophysics, 401, 227
Cesaroni R., Hofner P., Araya E., Kurtz S., 2010, Astronomy and Astrophysics, 509, A50
Cesaroni R., Hofner P., Walmsley C. M., Churchwell E., 1998, Astronomy and Astrophysics, 331, 709

Codella C., Beltrán M. T., Cesaroni R., Moscadelli L., Neri R., Vasta M., Zhang Q., 2013, Astronomy and Astrophysics, 550, A81
Codella C., Testi L., Cesaroni R., 1997, Astronomy and Astrophysics, 325, 282
Collings M. P., Anderson M. A., Chen R., Dever J. W., Viti S., Williams D. A., McCoustra M. R. S., 2004, Monthly Notices of the RAS, 354, 1133
Defrees D. J., McLean A. D., Herbst E., 1985, Astrophysical Journal, 293, 236
Fontani F., Pascucci I., Caselli P., Wyrowski F., Cesaroni R., Walmsley C. M., 2007, Astronomy and Astrophysics, 470, 639
Forster J. R., Caswell J. L., 1989, Astronomy and Astrophysics, 213, 339
Fuente A., Cernicharo J., Caselli P., McCoey C., Johnstone D., Fich M., van Kempen T., Palau A., Yildiz U. A., Tercero B., López A., 2014, ArXiv e-prints
Furuya R. S., Cesaroni R., Codella C., Testi L., Bachiller R., Tafalla M., 2002, Astronomy and Astrophysics, 390, L1
Furuya R. S., Cesaroni R., Shinnaga H., 2011, Astronomy and Astrophysics, 525, A72
Furuya R. S., Kitamura Y., Wootten A., Claussen M. J., Kawabe R., 2005, Astronomy and Astrophysics, 438, 571
Garay G., Lizano S., 1999, Publications of the ASP, 111, 1049
Garay G., Moran J. M., Rodriguez L. F., Reid M. J., 1998, Astrophysical Journal, 492, 635
Garay G., Reid M. J., Moran J. M., 1985, Astrophysical Journal, 289, 681
Garrod R. T., Weaver S. L. W., Herbst E., 2008, Astrophysical Journal, 682, 283
Gaume R. A., Mutel R. L., 1987, Astrophysical Journal, Supplement, 65, 193
Gibb A. G., Wyrowski F., Mundy L. G., 2004, Astrophysical Journal, 616, 301
Halfen D. T., Apponi A. J., Woolf N., Polt R., Ziurys L. M., 2006, Astrophysical Journal, 639, 237
Hatchell J., Thompson M. A., Millar T. J., MacDonald G. H., 1998, Astronomy and Astrophysics, 338, 713
Herbst E., van Dishoeck E. F., 2009, Annual Review of Astron and Astrophys, 47, 427
Ho P. T. P., Haschick A. D., 1986, Astrophysical Journal, 304, 501
Hoffman I. M., Goss W. M., Palmer P., Richards A. M. S., 2003, Astrophysical Journal, 598, 1061
Hofner P., Churchwell E., 1996, Astronomy and Astrophysics, Supplement, 120, 283
Hollis J. M., Lovas F. J., Jewell P. R., 2000, Astrophysical Journal, Letters, 540, L107
Huntress Jr. W. T., Mitchell G. F., 1979, Astrophysical Journal, 231, 456
Isokoski K., Bottinelli S., van Dishoeck E. F., 2013, Astronomy and Astrophysics, 554, A100
Jørgensen J. K., Favre C., Bisschop S. E., Bourke T. L., van Dishoeck E. F., Schmalzl M., 2012, Astrophysical Journal, Letters, 757, L4
Keto E., 2002, Astrophysical Journal, 568, 754
Keto E., Wood K., 2006, Astrophysical Journal, 637, 850
Keto E. R., Ho P. T. P., Haschick A. D., 1988, Astrophysical Journal, 324, 920
Keto E. R., Ho P. T. P., Reid M. J., 1987, Astrophysical Journal, Letters, 323, L117
Khlifi M., Paillous P., Bruston P., Raulin F., Guillemin J. C., 1996, Icarus, 124, 318
Klaassen P. D., Wilson C. D., Keto E. R., Zhang Q., 2009, Astrophysical Journal, 703, 1308
Kolpak M. A., Jackson J. M., Bania T. M., Clemens D. P., Dickey J. M., 2003, Astrophysical Journal, 582, 756
López-Sepulcre A., Codella C., Cesaroni R., Marcelino N., Walmsley C. M., 2009, Astronomy and Astrophysics, 499, 811
Lovas F. J., Dragoset R. A., 2004, Technical report, NIST Recommended Rest Frequencies for Observed Interstellar Molecular Microwave Transitions - 2002 Revision, (version 2.0.1), `http://physics.nist.gov/restfreq`. National Institute of Standards and Technology, Gaithersburg, MD.
Maxia C., Testi L., Cesaroni R., Walmsley C. M., 2001, Astronomy and Astrophysics, 371, 287
McKee C. F., Tan J. C., 2002, Nature, 416, 59
McKee C. F., Tan J. C., 2003, Astrophysical Journal, 585, 850
Modica P., Palumbo M. E., 2010, Astronomy and Astrophysics, 519, A22
Mookerjea B., Casper E., Mundy L. G., Looney L. W., 2007, Astrophysical Journal, 659, 447
Moscadelli L., Goddi C., Cesaroni R., Beltrán M. T., Furuya R. S., 2007, Astronomy and Astrophysics, 472, 867
Müller H. S. P., Schlöder F., Stutzki J., Winnewisser G., 2005, Journal of Molecular Structure, 742, 215
Occhiogrosso A., Viti S., Modica P., Palumbo M. E., 2011, Monthly Notices of the RAS, 418, 1923
Ohishi M., McGonagle D., Irvine W. M., Yamamoto S., Saito S., 1994, Astrophysical Journal, Letters, 427, L51
Olmi L., Cesaroni R., Hofner P., Kurtz S., Churchwell E., Walmsley C. M., 2003, Astronomy and Astrophysics, 407, 225
Olmi L., Cesaroni R., Neri R., Walmsley C. M., 1996, Astronomy and Astrophysics, 315, 565
Palla F., Stahler S. W., 1993, Astrophysical Journal, 418, 414
Pickett H. M., Poynter R. L., Cohen E. A., Delitsky M. L., Pearson J. C., Müller H. S. P., 1998, Journal of Quantitiative Spectroscopy and Radiative Transfer, 60, 883
Plume R., Jaffe D. T., Evans II N. J., 1992, Astrophysical Journal, Supplement, 78, 505
Pratap P., Megeath S. T., Bergin E. A., 1999, Astrophysical Journal, 517, 799
Rawlings J. M. C., Hartquist T. W., Menten K. M., Williams D. A., 1992, Monthly Notices of the RAS, 255, 471
Remijan A., Shiao Y.-S., Friedel D. N., Meier D. S., Snyder L. E., 2004, Astrophysical Journal, 617, 384
Remijan A. J., Markwick-Kemper A., ALMA Working Group on Spectral Line Frequencies 2007, in American Astronomical Society Meeting Abstracts Vol. 39 of Bulletin of the American Astronomical Society, Splatalogue: Database for Astronomical Spectroscopy. p. 132.11
Roberts J. F., Rawlings J. M. C., Viti S., Williams D. A., 2007, Monthly Notices of the RAS, 382, 733
Snyder L. E., Lovas F. J., Hollis J. M., Friedel D. N., Jewell P. R., Remijan A., Ilyushin V. V., Alekseev E. A., Dyubko

S. F., 2005, Astrophysical Journal, 619, 914
Sofia U. J., Meyer D. M., 2001, Astrophysical Journal, Letters, 554, L221
Sollins P. K., Ho P. T. P., 2005, Astrophysical Journal, 630, 987
Turner B. E., Apponi A. J., 2001, Astrophysical Journal, Letters, 561, L207
Vig S., Cesaroni R., Testi L., Beltrán M. T., Codella C., 2008, Astronomy and Astrophysics, 488, 605
Viti S., Caselli P., Hartquist T. W., Williams D. A., 2001, Astronomy and Astrophysics, 370, 1017
Viti S., Collings M. P., Dever J. W., McCoustra M. R. S., Williams D. A., 2004, Monthly Notices of the RAS, 354, 1141
Viti S., Williams D. A., 1999, Monthly Notices of the RAS, 305, 755
Wakelam V., Caselli P., Ceccarelli C., Herbst E., Castets A., 2004, Astronomy and Astrophysics, 422, 159
Wakelam V., Loison J.-C., Herbst E., Talbi D., Quan D., Caralp F., 2009, Astronomy and Astrophysics, 495, 513
Walsh A. J., Burton M. G., Hyland A. R., Robinson G., 1998, Monthly Notices of the RAS, 301, 640
Wilson T. L., Rood R., 1994, Annual Review of Astron and Astrophys, 32, 191
Wood D. O. S., Churchwell E., 1989, Astrophysical Journal, Supplement, 69, 831
Woodall J., Agúndez M., Markwick-Kemper A. J., Millar T. J., 2007, Astronomy and Astrophysics, 466, 1197
Woods P. M., Kelly G., Viti S., Slater B., Brown W. A., Puletti F., Burke D. J., Raza Z., 2012, Astrophysical Journal, 750, 19
Wu Y., Qin S.-L., Guan X., Xue R., Ren Z., Liu T., Huang M., Chen S., 2009, Astrophysical Journal, Letters, 697, L116